d/Collection

Ph.D. DISSERTATION

Development of 3D Printing-based Customized Optical Components for Display and Imaging System Applications

디스플레이 및 이미징 시스템으로의 응용을 위한
3D 프린팅 기반 맞춤형 광학 요소의 개발

FEBRUARY 2021

DEPARTMENT OF ELECTRICAL AND
COMPUTER ENGINEERING
COLLEGE OF ENGINEERING
SEOUL NATIONAL UNIVERSITY

SEUNGHWAN LEE

Development of 3D Printing-based Customized Optical Components for Display and Imaging System Applications

디스플레이 및 이미징 시스템으로의 응용을 위한 3D 프린팅 기반 맞춤형 광학 요소의 개발
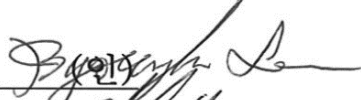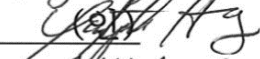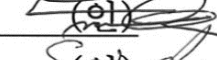
지도교수 홍 용 택

이 논문을 공학박사 학위논문으로 제출함
2021 년 2 월

서울대학교 대학원
전기 · 정보 공학부
이 승 환

이승환의 공학박사 학위논문을 인준함
2021 년 2 월

위 원 장	이 병 호	(인)
부위원장	홍 용 택	(인)
위 원	정 윤 찬	(인)
위 원	유 승 협	(인)
위 원	정 승 준	(인)

Abstract

Development of 3D Printing-based Customized Optical Components for Display and Imaging System Applications

SEUNGHWAN LEE

DEPARTMENT OF ELECTRICAL AND COMPUTER ENGINEERING

COLLEGE OF ENGINEERING

SEOUL NATIONAL UNIVERSITY

Generally, the manufacturing process is divided into the subtractive (top-down) type and additive type (bottom-up). Among them, the additive manufacturing process has attracted a lot of attention because it can manufacture products with complex shapes in a low-cost and short-time process. In particular, three-dimensional (3D) printing is a representative method, which has already been commercialized in the field of mechanical components and biomedical organ. However, it remains in the research and development step in the field of electronic devices and optical components. Especially, although 3D printed optical components including microlens and color filter are expected to be widely used in display and imaging systems, it is still under investigation for commercialized products, and there are limitations in terms of materials, length scale, shape, and practical applications of components. Therefore, to overcome these issues, it is required for investigating and expanding the potential

usefulness for 3D printed optical components in display and imaging systems to achieve better performance, productivity, and usability in three aspects. First, it should be possible to manufacture structures with a wide range of length scales from micrometer to centimeter through various 3D printing methods. Second, complex shapes such as free-from curved surfaces and hierarchical structures should be easily fabricated. Third, it is necessary to add functionality by manufacturing structures in which tunable functions are introduced using soft materials like an elastomer.

Based on the above motivations, 3D printing-based customized optical components for display and imaging system applications are introduced in this dissertation. 3D printed optical components are classified into three types and their applications are showed to verify the scalability of 3D printing: macro-scale, microscale, and hierarchical macro/micro-scale. As macro-scale printed optical components, lens and mirror which are the most basic optical components are selected. The lens is fabricated by a pneumatic-type dispensing method with the form of a cylindrical pair and adopted for demonstration of seamless modular flat panel display. Besides, a seamless modular curved-edge display is also demonstrated with a mirror, which is fabricated from fused deposition modeling (FDM)-type 3D printed mold. By simply attaching a printed lens or mirror onto the seam of the modular display, it is possible to secure seamless screen expansion technology with the various form factor of the display panel. In the case of micro-scale printed optical components, the color-convertible microlens is chosen, which act as a color converter and light extractor simultaneously in a light-emitting diode (LED). By electrohydrodynamic (EHD) printing of quantum dot (QD)/photocurable polymer composite, QD-embedded hemispherical lens shape structures with various sizes are

fabricated by adjusting printing conditions. Furthermore, it is applied to a blue micro-LED array for full-color micro-LED display applications. Finally, a tunable bio-inspired compound (BIC) eyes structure with a combination of dispensing and a dry-phase rubbing process is suggested as a hierarchical macro/micro-scale printed optical components. A hemispherical macrolens is formed by the dispensing method, followed by a dry-phase rubbing process for arranging micro particles in monolayer onto the curved surface of the macrolens. This hierarchical structure is replicated in soft materials, which have intrinsic stretchability. Microlens array is formed on the surface of the macrolens and acts as a rigid island, thereby maintaining lens shape, resolution, and focal length even though the mechanical strain is applied to overall hierarchical structures and the shape of the macrolens is changed.

The primary purposes of this dissertation are to introduce new concepts of the enabling technologies for 3D printed optical components and to shed new light on them. Optical components can be easily made as 3D printing equipment becomes cheaper and more precise, so the field of 'Consumer optics' or 'Do it yourself (DIY) optics' will be gradually expanded on deformable and multi-scale optics. It is expected that this dissertation can contribute to providing a guideline for utilizing and customizing 3D printed optical components in next-generation display and imaging system applications.

Keyword: 3D printing, optical component, display and imaging system, lens, mirror, color filter, bio-inspired compound eyes

Student Number: 2014-21610

Contents

List of Tables

List of Figures

Chapter 1

Introduction

1.1. Manufacturing Process

Manufacturing is a field of making necessary physical products for human life, contributing greatly to maintaining modern society. Since the manufacturing industry has a large portion of the national economy, it is important to determine which methods can be used to manufacture products efficiently. Although there are many different methods for manufacturing products, these can be classified into two parts: subtractive manufacturing process and additive manufacturing process. The subtractive manufacturing process refers to the method of forming a structure by removing (top-down) materials. General methods of mechanically subtractive manufacturing processes include milling, drilling, and grinding. These methods are mostly utilized for mass production due to their high precision and productivity. In addition, in the conventional semiconductor process, which is a kind of chemical reaction, photolithography and etching are included in the subtractive manufacturing process. Since semiconductors are crucial components of electronic devices, the subtractive manufacturing process is an indispensable technology for the growth of the Internet of Things (IoT). However, the subtractive manufacturing process has
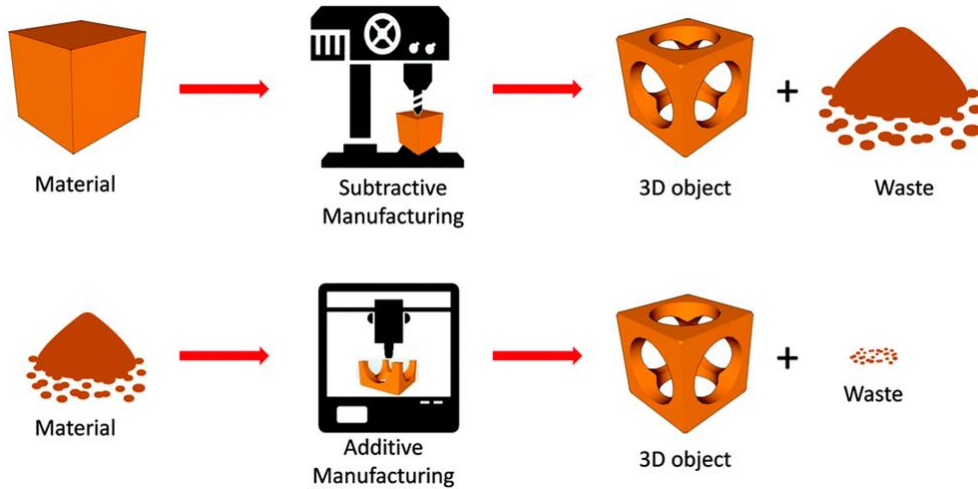
Figure 1.1. Comparison between the subtractive and additive manufacturing process [1].

the disadvantages such as requirements of bulky and expensive maintenances, long process time, heavy waste of materials, and difficulty in obtaining three-dimensional (3D) complex structures such as volumetric electrical circuit, mannequin, and building model.

The additive manufacturing process, which is also called 3D printing, is a method of building a structure (bottom-up) by adding materials from micro/nanometer scales. Since it is not a method of removing materials, waste of materials can be reduced, and it has the advantage of being facile to create 3D complex structures, unlike the subtractive manufacturing process [1], as shown in Fig. 1.1. Furthermore, due to its simple maintenance requirement and short process time, it is widely applied to evaluate products with prototypes in the development stage, thereby saving costs for production. Although there are disadvantages that the commercially available materials are still limited to low young's modulus materials
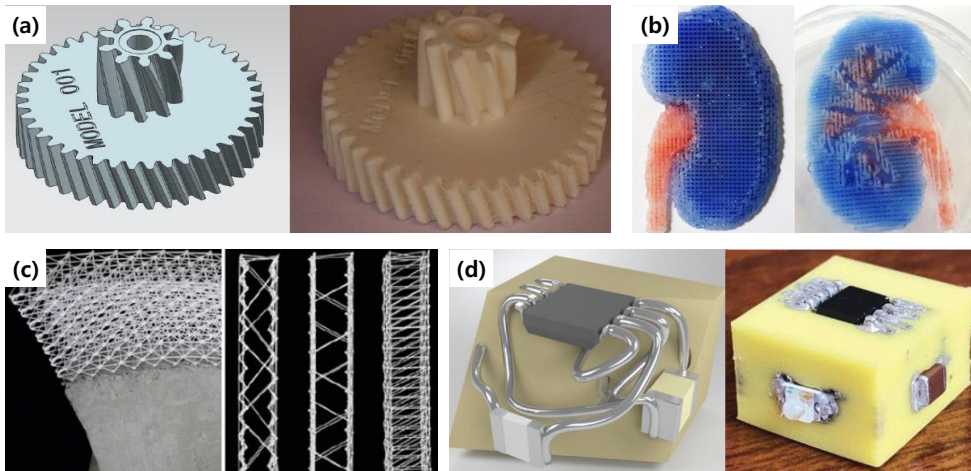
Figure 1.2. Promising applications of additive manufacturing: (a) mechanical components [2], (b) biomedical organ [5], (c) architectural modeling [4], and (d) electrical circuits [3].

like plastic or rubber and the size resolution is low as tens or hundreds micrometers, researches on additive manufacturing process have been gradually increased. Accordingly, 3D printing for hard materials including metals and ceramics has appeared, and the size resolution has also reached several micrometers. 3D printing is highly expected to be applied not only to the manufacturing industry including mechanical [2] and electrical components [3] but also to various fields such as architectural modeling [4] and biomedical organ [5], as shown in Fig. 1.2. The use of 3D printing will expand design freedom and the base of the 'Do it yourself (DIY)' project where consumers can customize the products with their preference. That's why many research groups and companies are paying attention and investigating the additive manufacturing process. In the next section, the methods, characteristics, and promising applications of the additive manufacturing processes are described in detail.

1.2. Additive Manufacturing

Figure 1.3 presents the general steps of additive manufacturing. Additive manufacturing is conducted by slicing a structure designed or captured by computer-aided design (CAD) to convert it into processable data, followed by transferring data to a 3D printer [6]. Depending on the fabrication method, material, and resolution, there have been two main approaches for additive manufacturing: Ink-based and light-based additive manufacturing [7], as shown in Fig. 1.4.

(1) Ink jetting-based additive manufacturing: This strategy focuses on patterning material in the form of printable inks. There are representative methods such as fused deposition modeling (FDM) [8] and direct ink writing (DIW) [9].

FDM is a method of manufacturing by melting thermoplastic materials like polylactic acid (PLA) and acrylonitrile butadiene styrene (ABS) in the form of filaments at high temperatures and then extruding them in layer-by-layer stacking.
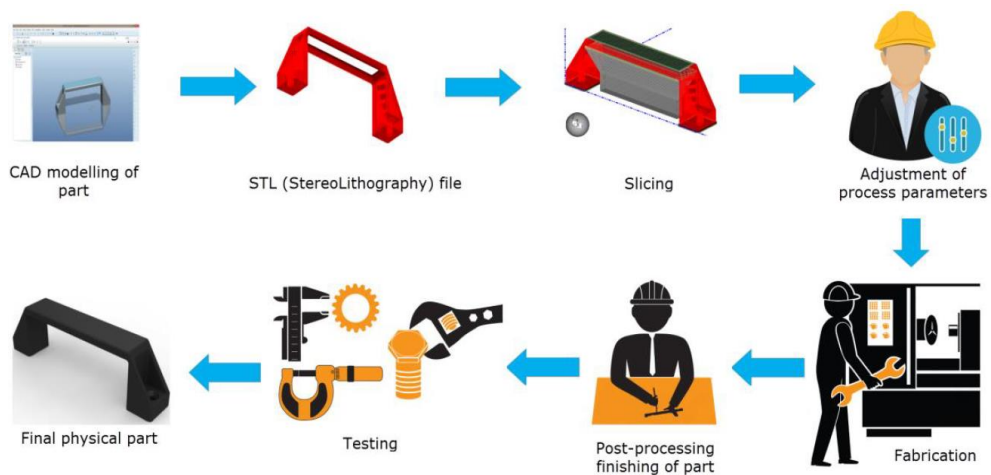
Figure 1.3. Overview and principle of additive manufacturing [6].

4

Due to the short process time, low cost of materials, and simple maintenance, this method is the most selected for commercialized 3D printer. However, there are disadvantages in that the available materials are limited, and post-processing is required to obtain a smooth surface due to the low size resolution of the FDM method and protruding parts on the printed structures.

DIW printing, which is one of the alternatives to FDM printing, is a method of jetting liquid ink directly and has a wide range of available materials including electrical, optical, and biological materials, and a low minimum feature size down to several micrometers. The representative methods of DIWs are the piezoelectric and pneumatic type that can allow single or multiple nozzle printing on the various surface. Furthermore, nanostructures can also be fabricated through electrohydrodynamic (EHD) printing [10] in which liquid is jetted by overcoming a critical limit of electrical potential by applying a high voltage between the nozzle and the target substrate.

(2) Light curing-based additive manufacturing: This strategy allows to use of light to sculpt desired structures. As representative methods, stereolithography (SLA) [11] and selective laser sintering (SLS) [12] are the widely used approaches.

In SLA, a photocurable liquid is polymerized by ultraviolet (UV) light, followed by repeating the same process layer-by-layer until the desired structure is completed. The printer resolution of SLA is similar to that of FDM, so post-processing is required to flatten the surface of structures. To solve this problem, two-photon polymerization (2PP) [13] have been investigated to provide high resolution to SLA type printer in recent years. However, there is a tradeoff between printer resolution and throughput because as the ink volume unit is smaller, the processing
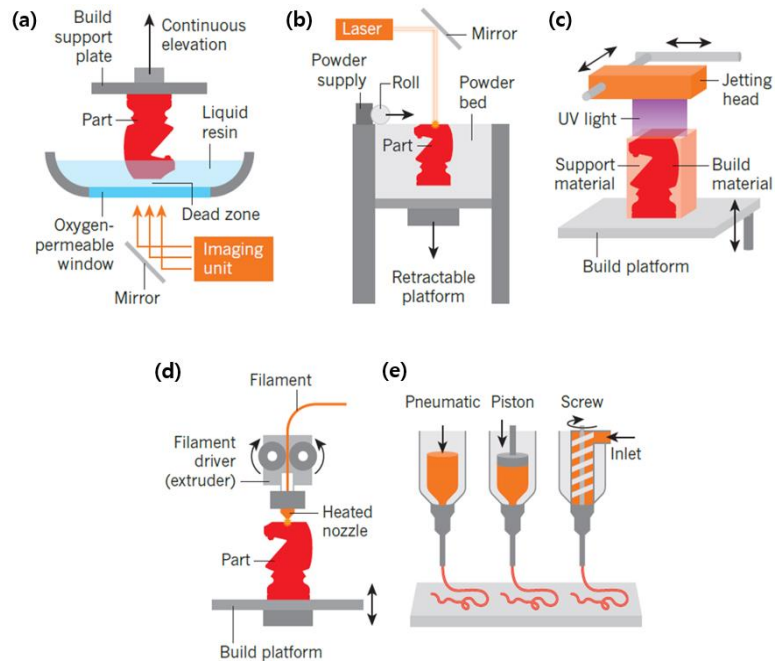
Figure 1.4. Types of additive manufacturing: (a) stereolithography, (b) selective laser sintering, (c) photocurable inkjet printing, (d) fused deposition modeling, and (e) direct ink writing [7].

time becomes longer. For this reason, the 2PP is mainly utilized when fabricating nano-scale structures, and SLA is used when fabricating micro-scale structures and focusing on a short process time.

SLS is a method for locally heating and fusing polymer particles with laser, followed by repeating the same process layer-by-layer until the desired structure is completed. The minimum feature size is determined by the size of particles and is approximately tens of micrometers. It has the advantages that the remaining particles after the process are recycled and hard material can be utilized for printing, thereby requiring no support structures. However, since laser and powder inhalers should be needed, the overall maintenance becomes expensive.

Since there are various types of additive manufacturing processes as described above, researchers should select appropriate approaches for their purpose. In some cases, hybridizing methods combining inkjet and light-based types can be adopted for achieving the advantages of each method simultaneously.

Currently, the fields where additive manufacturing is widely applied are mechanical components, architectural modeling, and biomedical organ. These are manufactured in macro-scale of several centimeters to meters and have been commercialized to some extent. Most of them are large-sized structures where the surface roughness is not critical, so these are mainly produced by the FDM method. In small-scale applications like microelectromechanical systems (MEMS) [14], mechanical components are fabricated by inkjet printing.

Other potential applications for additive manufacturing are electronic devices and optical components, which are typically fabricated by a subtractive manufacturing process. When making them in additive manufacturing, these are limited to research or prototype production. Their length scales are generally on the order of several micrometers to centimeters, and these show many different aspects in the required materials, minimum feature size, and surface properties compared to these of the commercialized field. In the case of electronic components, it has reached the level of manufacturing short-channel transistors shorter than 10 μm channel length with only inkjet printing [15]. However, although there have been several reports about the fabrication and evaluation of additive manufactured optical components such as lenses [16], prisms [17], and mirrors [18], there are few cases suggesting their practical applications. The development status and considerations of additive manufactured optical components will be discussed in the next session.

1.3. Printed Optical Components

Figure 1.5 shows the roadmap of printed optoelectronics components [19]. A representative example is one-drop-fill (ODF) technology [20] which achieved great success in the liquid crystal display (LCD). Also, although microlenses and color filters are generally fabricated by photolithography, researches for applying the inkjet printing method have been conducted [21], as shown in Table 1.1. The reason for adopting inkjet printing is that process steps are reduced, and materials can be used efficiently. Printing of quantum dot (QD) layer for the color filter in LCD, organic light-emitting diodes (OLEDs), and the micro-LED display is a widely commercialized example. However, there are few cases of applying printed optical components other than the display panel, and the manufactured scale is also limited to the pixel size. Therefore, attempts to fabricate optical components have been ongoing to expand scales and applications, as shown in Fig. 1.6. Unlike conventional applications including mechanical components and building modeling, additional considerations only when manufacturing optical components are as follows.

(1) Highly transparent or reflective materials: In displays and imaging devices, the transmittance of the materials for lens or prism should be higher than 80 % in the visible or infrared light wavelength, and the printable materials for practical applications include acrylate-based photocurable optical adhesive, polydimethylsiloxane (PDMS), and polymethylmethacrylate (PMMA). Reflective structures like mirrors can be obtained by vapor deposition or powder sintering of materials such as aluminum (Al) and silver (Ag), which show high reflectance over 80 % in the visible or infrared light wavelength.
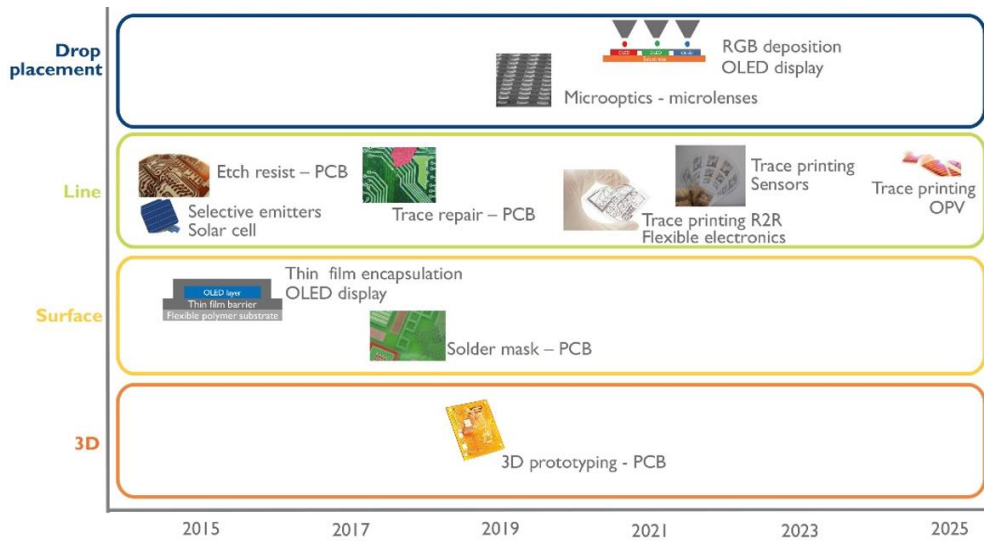
Figure 1.5. Roadmap of additive manufactured optoelectronic components according to dimensions and functions [19].

Application	Requirements	Status
Organic TFE	WVTR, planarization	In mass production
RGB OLED	HIL/HTL/EML	Under development
Color conversion (BOLED, microLED)	Color uniformity	Under development
OCA/Filler	1~3 μm thin film, high refractive index	Under investigation
Microlens, Line array	High refractive index	Under investigation
QDEL/QDLED	HIL/HTL/EML, uniformity	Under investigation
Color filter	Uniformity	Under investigation
Pixel well bank	$\leq 20\ \mu m$ width	Limited to ~15 μm width
Polyimide substrate	Patterned for lift-off ease	Switching cost justification
QD encapsulation	Protective layer	Single SiN CVD layer
Inorganic TFE	WVTR	Need soluble inks
Black matrix	High accuracy $\leq 1\ \mu m$	Lithography more appropriate
Hardcoat	Scratch resistant, oleophobic	Switching cost justification

Table 1.1. Emerging applications, requirements, and status of inkjet printing in the display and imaging devices industry [21].
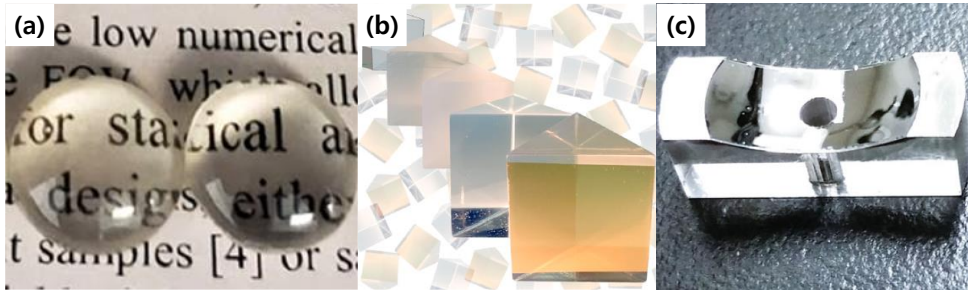
Figure 1.6. Printed optical components: (a) aspherical lens [16], (b) Au-coated prism [17], and (c) Al-coated mirror [18].

(2) Surface smoothness: It is difficult to fabricate the optical components with additive manufacturing because their surface roughness should be satisfied with tens of nanometer, which is much lower than that of the minimum feature size of a 3D printer with tens of micrometers. Therefore, post-processing such as polishing, coating, and chemical processing should be conducted for surface planarization.

Since there are issues that are only applicable to printed optical components, finding the proper optical materials and post-processing method is still a great challenge in optics, photonics, and related academics and industries.

1.4. Motivation and Organization of Dissertation

Although the fabrication and performance of printed optical components have been studied by many research groups in recent years, it is still under investigation for prototypes or commercialized products. There are limitations in terms of printable materials, length scale, shape, and practical applications of components. Therefore, to overcome these issues, it is required for investigating and expanding the potential usefulness for printed optical components intensively, especially in display and imaging systems, to achieve better performance, productivity, and usability in three aspects as follows.

(1) Wide range of length scale: it should be possible to manufacture structures with a wide range of length scales from micrometer to centimeter through various 3D printing methods.

(2) Complex structures: unconventional shapes such as free-from curved surfaces and hierarchical structures, which are difficult to be formed by subtractive manufacturing process, should be easily fabricated.

(3) Tunable functionality: it is necessary to add the new functionality by manufacturing structures in which tunable functions are introduced using soft materials like rubber instead of rigid materials.

Based on motivations as mentioned above, this dissertation consists of five chapters including Introduction and Conclusion. Several types of printed optical components and their display and imaging system applications are presented to verify the scalability of printing in each chapter: macro-scale, micro-scale, and hierarchical macro/micro-scale, as shown in Table. 1.2.

Chapter 1 briefly describes the methods of additive manufacturing processes and issues when it is applied to the fabrication of optical components. Furthermore, three aspects to be considered for display and imaging devices applications of printed optical components are presented.

Chapter 2 introduces macro-scale printed optical components, and the lens and mirror are selected, which are the most basic optical components. The lens is fabricated by a pneumatic-type dispensing method with the form of a cylindrical pair and adopted for demonstration of seamless modular flat panel display. A seamless modular curved-edge display is also demonstrated with a mirror, which is fabricated from FDM-type 3D printed mold. By simply attaching a printed lens or mirror onto the seam of the modular display, it is possible to show the applicability of seamless screen expansion technology with the various form factor of display panels.

Chapter 3 presents micro-scale printed optical components, and a color-convertible microlens is chosen, which acts as a color converter and light extractor simultaneously in LED. By EHD printing of QD/photocurable polymer composite, QD-embedded hemispherical lens shape structures are formed with various sizes by adjusting printing conditions. Furthermore, it is applied to a blue micro-LED array for full-color micro-LED display applications.

Chapter 4 introduces a hierarchical macro/micro-scale printed optical components. As an example, a tunable bio-inspired compound (BIC) eyes structure with a combination of dispensing and a dry-phase rubbing process is suggested. A hemispherical macrolens is formed by the dispensing method, followed by a dry-phase rubbing process for assembling microparticles in monolayer onto the curved surface of the macrolens. This hierarchical structure is used as a template and is

replicated in soft materials, which has intrinsic stretchability. The microlens array is formed on the surface of the macrolens and acts as a rigid island, thereby maintaining lens shape and focal length even though the mechanical strain is applied to overall hierarchical structures and the shape of the macrolens is changed.

Finally, Chapter 5 summarizes the main concepts and achievements of this dissertation. Furthermore, the limitations and suggestions for future researches are also discussed in the field of printed optical components and their promising applications.
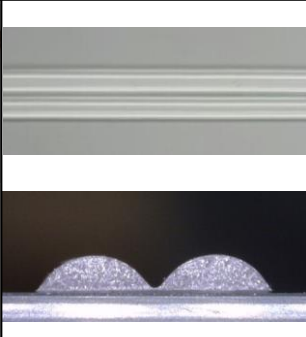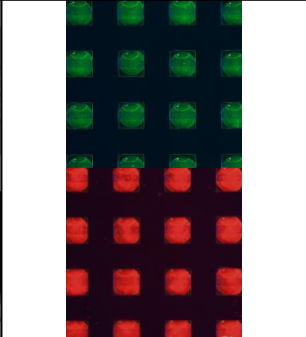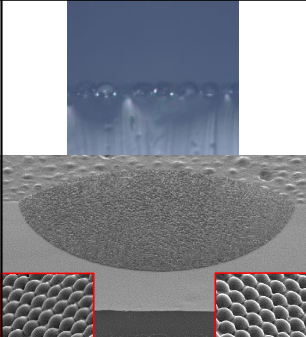
Component	Reflective type	Refractive type		
	Mirror	Lens	Color converter	Compound eyes
Image				
Fabrication method	Fused deposition modeling (FDM)	Dispensing	Electrohydrodynamic (EHD) printing	Dispensing / Dry-phase rubbing
Length scale	**Several mm (macro-scale)**		**Tens of μm (micro-scale)**	**Tens of μm / Several mm (macro/micro-scale)**
Material	Soft	Hard		Soft
Shape	Concave	Convex		Convex (Hierarchical)
Application	Display			Imaging
Chapter	**2**		**3**	**4**

Table 1.2. Organization of dissertation: 3D printing-based customized optical components for display and imaging system applications.

Chapter 2

Macro-scale Printed Optical Components

2.1. Introduction

This chapter introduces printed lens and mirror in macro-scale and their applications to seamless modular displays. The applications of macro-scale optical components in displays are suitable for products rather than internal devices, and examples include an LED package, light guide plate (LGP), and optical films [22]. However, there are few cases in which macro-scale optical components are utilized other than those mentioned above. Therefore, with the motivation to find other practical applications, implementing a seamless modular display is adopted as a case in which macro-scale optical components can be applied to display panels and fabricated with printing technology immediately.

The tiling of multiscreens are one of the key enabling technologies for large-area display applications through the arrangement of panels in the same plane. Due to the high cost and low production yield of large-area displays, this approach has been widely adopted in the display industry [23]. Furthermore, the tiling method is suitable for simply implementing modular displays by customizing the arrangement

of panels according to the place, the size of the space, and personal preferences. However, the mechanical frame around the panel, which is called the seam, prevents observers from watching a continuous image through modular displays. To demonstrate seamless modular images, several methods have been suggested, including overlapping the seam [24], reducing the width of the seam [25], and attaching optical components onto the seam [26, 27] for optical clocking. The first method is advantageous in that it only overlaps the edges of panels, but it has the disadvantages of increasing the thickness of the overall screen and requiring complex mechanical design for precise alignment of each panel. The second method is an approach to reduce the area of the gate driver region, but it is almost impossible to completely remove the seam due to the physical limitations of fining and redesigning the circuit system.

As an optical component that can be applied to the seam, the plano-convex lens is a representative example. This approach is to place a lens for covering the dark lines between light-emitting areas [28] and has also been applied to increase the power conversion efficiencies of the photovoltaic device by cloaking the contact fingers [29]. By attaching lens pair onto the seam directly, light emitted from the vicinity of the seam is refracted toward the seam, thereby optically concealing the seam and showing a continuous image, as shown in Fig. 2.1. Fabrication of proper shape of the lens is typically based on conventional microelectronic technology such as thermal reflow of photoresist [30], chemically wet etching [31], direct laser writing [32], and hot embossing [33]. These methods are time-consuming and involve high process costs associated with the vacuum systems, photolithography and etching [34]. In recent years, direct lens fabrication with liquid material has been
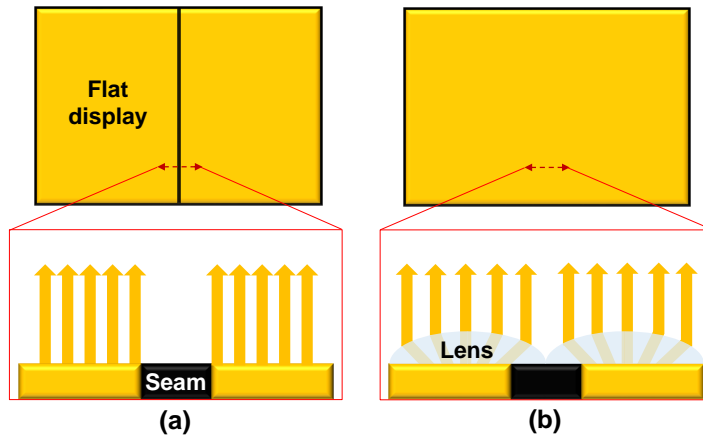
Figure 2.1. Schematic diagram of modular flat display (a) without and (b) with convex lens. The insets show cross-sectional view of displays [26].

employed as a promising, cost-effective method with a high degree of design freedom, including inkjet [35] and dispenser printing [36]. In the case of inkjet printing method, there is a limitation on the jetting of highly viscous liquid (> 20 mPa·s) [37]. It is difficult to fabricate a cylindrical lens [38] with a high aspect ratio, which is widely used for 3D displays [39] and laser beam focusing [40]. Dispenser printing is an alternative method to overcome the disadvantages of inkjet printing, and suitable for obtaining low-cost and high-performance lens. In chapter 2.2, a method for fabricating cylindrical lens pair (CLP) based on the dispenser printing is proposed for a seamless modular display application. The luminance distribution of seamless modular display is analyzed, followed by a demonstration of seam concealment to verify that the proposed method on display panel works excellently.

Although there is an advantage that the process is simple because it is fabricated by dispensing transparent optical adhesive directly onto the seam, a narrow viewing angle has been a bottleneck due to the limited available range of the virtual image

expanded by the lens. As an alternative to the refractive optical components, a waveguide can act as a transformation element of edge and corner images, thereby developing a zero-seam flat panel display module [27]. This study shows a wide range of viewing angles, but it is difficult to widely apply to large-area displays due to the high cost of optical fiber guides.

The seamless modular display technologies described so far have been applied only in flat panel displays. Displays with diverse form factors are required to provide a new user experience to the consumer. Curved-edge displays with flexible panels have been widely used in commercialized products for their widescreen view and aesthetic benefits due to the curvature of the edge [41]. In addition to large displays, small- to medium-sized displays such as smartphones and tablet computers can be tiled to form modular displays. It is possible to utilize curved-edge display panels as a part of a modular display because the seam of curved-edge displays is narrow [42]. However, the modular image is still has seen discontinuously. Therefore, seam concealment methods for curved-edge displays should be developed for the new form factors of modular displays. Utilization of a concave mirror, which has been used in various projection-type optical systems, including 3D displays [43], panoramic imaging [44], and laser beam scanners [45], is considered an option for demonstrating seamless modular curved-edge displays.

There is a need for a technique that makes it easier to fabricate optical components for seamless modular display applications. 3D printing has been adopted in various fields for rapid production, and optical components can be quickly fabricated as designed using 3D printing. Furthermore, molded optics are being employed in 3D printing for repeatable production of prototypes and parts that are
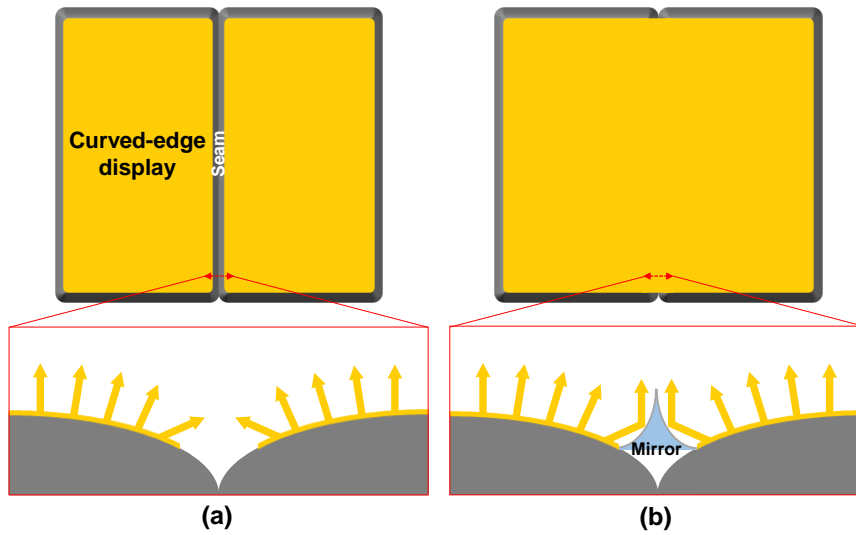
Figure 2.2. Schematic diagram of modular curved-edge display (a) without and (b) with concave mirror. The insets show cross-sectional view of displays.

difficult to fabricate by direct printing [46].

Based on the background mentioned above, a method for designing and fabricating a concave mirror as an optical component from a 3D printed mold is proposed for seamless modular curved-edge display applications in chapter 2.3. In Fig. 2.2, the concave mirror is placed between the curved-edge displays, concealing the seam and showing an overall continuous image by reflecting the image at the curved-edge area toward the observer direction. By investigating how the structure of the concave mirror affects the seamlessness according to geometric optics and parametric modeling based on the configuration of the curved-edge display system, image discontinuity between the curved-edge displays is shown to be mitigated. The luminance distribution and the viewing angle of the seamless modular curved-edge display are measured and analyzed to verify the seam concealment effect by the concave mirror.

2.2. Seamless Modular Flat Display with Printed Lens

2.2.1. Main Concept

Figure 2.3 represents the image-forming behavior of a plano-convex lens. The fabricated lens is a plano-convex type, which generates a virtual image of an object on opposite sides of the focal point when the object distance is shorter than the focal length. The image below the plano-convex lens is enlarged to cover the seam, thereby leading to the optical concealment effect. Based on the Gaussian lens formula, magnification can be expressed by

$$M = \frac{f}{t-f} \quad (t < f) \tag{2.1}$$
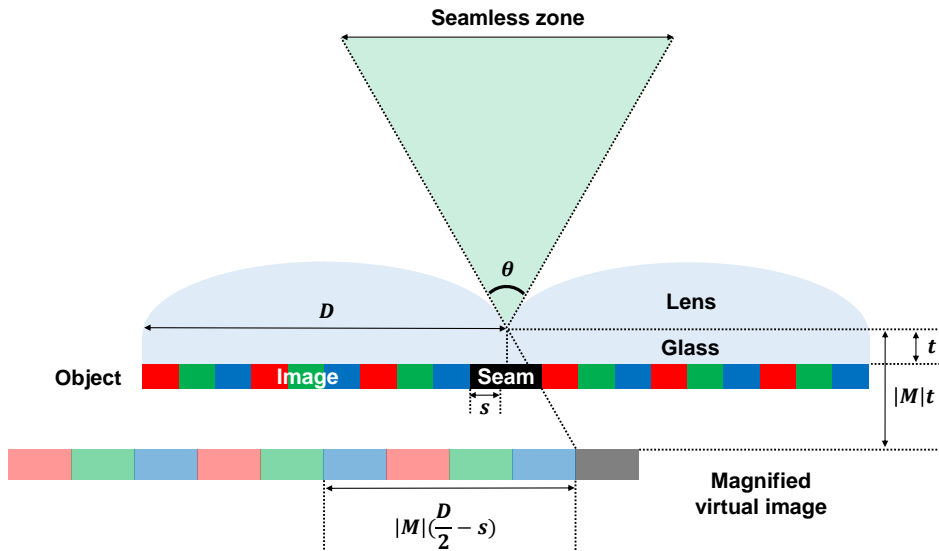
Figure 2.3. Image-forming behavior of plano-convex lens and principle of seamlessness appearance due to the magnified virtual image of the object generated by plano-convex lens [26].

where M, t, and f represent the magnification of lens, the thickness of glass and the focal length of lens, respectively. It is assumed that the fabricated plano-convex lens shows the negligible difference in a focal point between paraxial and marginal rays because the surface of lens is an aspherical form [47]. Besides, the lens formula can be applied for the aspherical refracting surface [48]. So although Eq. (2.1) is derived under the assumption of paraxial rays, it is suitable for the theoretical description of the seamless modular display system. To calculate the magnification, the focal length should first be calculated from the surface profile of the lens by ray-tracing simulation [49] or be measured by collimator [50]. Then, the magnification of the lens can be calculated by inserting the focal length and the thickness of glass into Eq. (2.1). The viewing angle of a seamless modular display is defined as the theoretical maximum angular range at which the seam is not observed. According to the principle of seamlessness presented in Fig. 2.3, the viewing angle is derived as the following equation:

$$\theta = 2arctan\left[\frac{|M|(D-2s)-D}{2|M|t}\right] \tag{2.2}$$

where θ is the viewing angle, D is the diameter of the lens, and s is the half of seam width. The viewing angle is also related to the power of the lens which can be represented by the f-number. Generally, the f-number is defined as

$$F = \frac{f}{D} \tag{2.3}$$

where F is the f-number of the lens. As a result, Eq. (2.2) can be rewritten in terms of F as the following equation:

$$\theta = 2arctan\left[\frac{t-2Fs}{2Ft}\right] \tag{2.4}$$
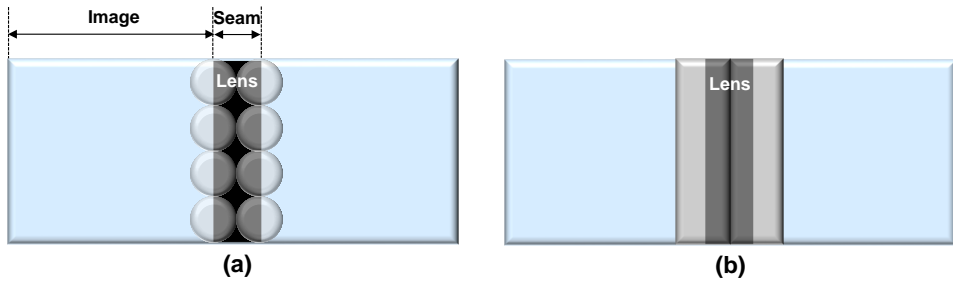
Figure 2.4. Fill factor of lens array for seam concealment effect: (a) spherical lens array and (b) cylindrical lens pair.

Thus, the viewing angle from the variables associated with a seamless modular display can be determined according to Eq. (2.1) - (2.4).

The method presented here provides the capabilities of engineering geometric parameters of a cylindrical lens and achieving a maximum fill factor (FF) of lens array, which is important to achieve complete seam removal. In this case, FF is defined as the ratio of seam area covered by a lens to total seam area, which is determined by packing density and arrangement of each lens. If FF is not 100 %, the part of the seam that is not covered by the lens is observed, as shown in Fig. 2.4 (a). In Fig. 2.4 (b), all seam area is concealed by CLP due to its FF around 100 % [51]. Generally, high FF enhances the optical performance of the lens array in the optical imaging and detection system [32]. With this motivation, the CLP is used for seamless modular display application.

2.2.2. Experimental Section

Figure 2.5 shows the fabrication process of a CLP. As a lens material, Norland Optical Adhesive 63 (NOA 63, Norland Products), which has been widely used as UV curable liquid polymer, is selected due to its high refractive index (1.56), high transparency (~ 99 % at visible light wavelength), fast UV-curing property in ambient condition, and low cost [52]. Especially, it has a high line pattern fidelity when continuously dispensed onto the glass substrate, showing the advantage of cylindrical lens formation. Another candidate material for fabricating cylindrical lens PDMS, which has been used for fabricating elastomeric lens array [49]. However, since PDMS has a property of rapidly spreading onto the glass at room temperature and has to be thermally cured for a long time, it is difficult to obtain a cylindrical lens of the desired shape directly.

At first, a pre-cleaned glass substrate is placed on a stage of an automatic dispenser (SHOTmini 200Sx, Musashi Engineering). The dispenser is on a laboratory table with small vibration to keep it flat, thereby fixing the nozzle and the substrate. The height of the nozzle is controlled by a controller that can program the jetting position, and it is maintained at 200 µm in the whole fabrication process. After placing the substrate, NOA 63 is jetted continuously through a metal nozzle with 900 µm diameter in contact with the substrate in a straight path mode. With straight path mode, the length of the cylindrical lens can be controlled freely within the size of the stage. In the experiment, the cylindrical lens is fabricated with 15 cm length. The printed cylindrical lens is cured immediately for 1 min with the 365 nm wavelength UV light having an intensity of 7 mW/cm^2 by using a portable UV lamp (LF206LS,
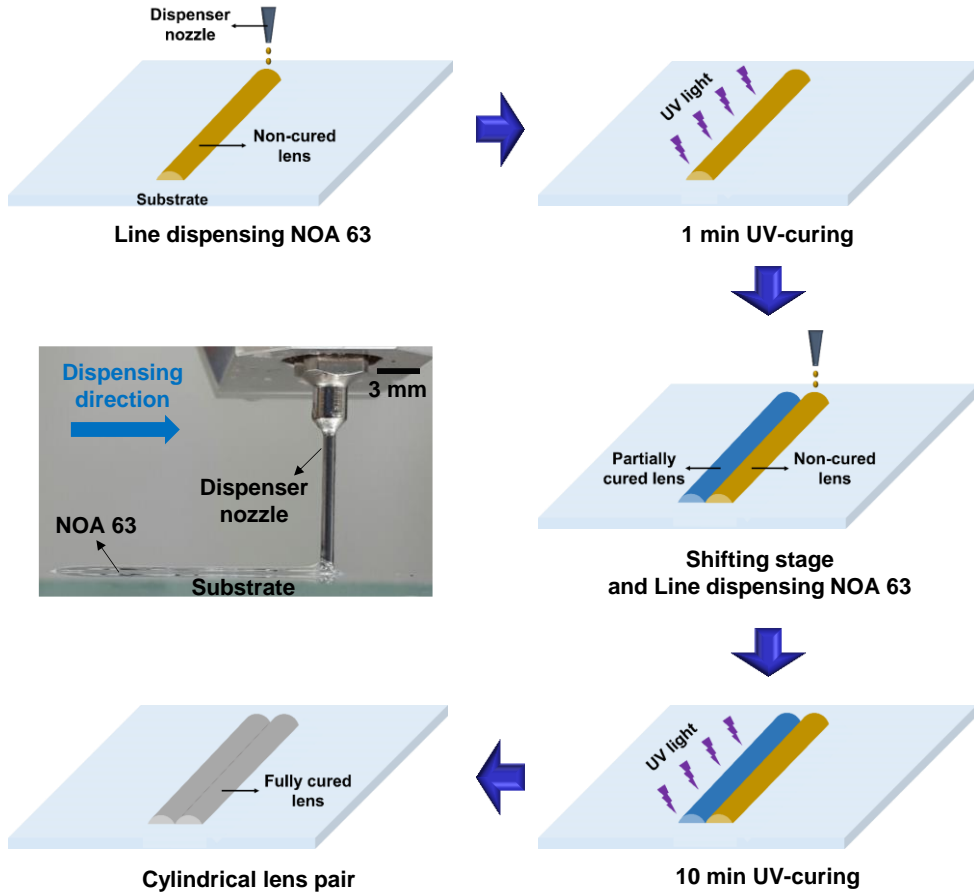
Figure 2.5. Fabrication process of a CLP with the dispenser printing method. The inset shows the continuous dispensing of NOA 63 [26].

UVITEC Cambridge). After 1 min UV-curing, the stage is moved by the diameter of the cylindrical lens, and subsequently, another cylindrical lens under the same jetting condition is formed as in the previous fabrication step, followed by full curing for 10 min. It is noted that both cylindrical lenses are not merged because the shape of the cylindrical lens in the first step is already fixed in a solid phase through the partial curing process.

The shapes of the cylindrical lens are investigated by a 3D surface profiler (μSurf, NanoFocus) with confocal microscope mode. The cross-section view is captured by a digital microscope (AM-413TL, Dino-Lite). The focal lengths of each cylindrical lens are calculated from the measured surface profiles by ray-tracing simulation software (LightTools 8.5, Synopsys). The luminance simulation and measurement of backlight with CLP and those without CLP are performed to investigate the effect of CLP for a seamless modular display. The luminance simulation with ray-tracing simulation software is conducted which is utilized for calculating the focal length of the cylindrical lens. The optical system is constructed by using a commercial white LED backlight module (MEC-12889, Mechasolution), seam, glass, and CLP according to the design variables set on the simulation. The seam is formed by attaching a transparent polymer sheet printed with a black matrix onto the LED backlight and the configured system is mounted to the home-made rotating stage perpendicular to the surface of the optical table for measurement. The luminance is measured along with the position of LED backlight in 500 μm intervals in the x-direction by using the luminance meter (CS-200, Konica Minolta) at a distance of 300 mm. At the same measurement position, the luminance is measured three times and the average value is calculated. For actual image, the system is constructed by attaching the glass on which the optimized CLP is formed to the commercial monitor where the image with the seam is displayed. The viewing distance is 500 mm and the magnification by capturing camera is 4.

2.2.3. Results and Discussion

In the fabrication process, the geometric shape of the cylindrical lens can be controlled by adjusting jetting conditions. Figure 2.6 (a)-(c) show the cross-sectional profiles of the cylindrical lens with different jetting conditions. Since both ends of the cylindrical lens are the starting and ending position of jetting where cross-section profile inhomogeneity appears, the cross-section profile at the center position of the
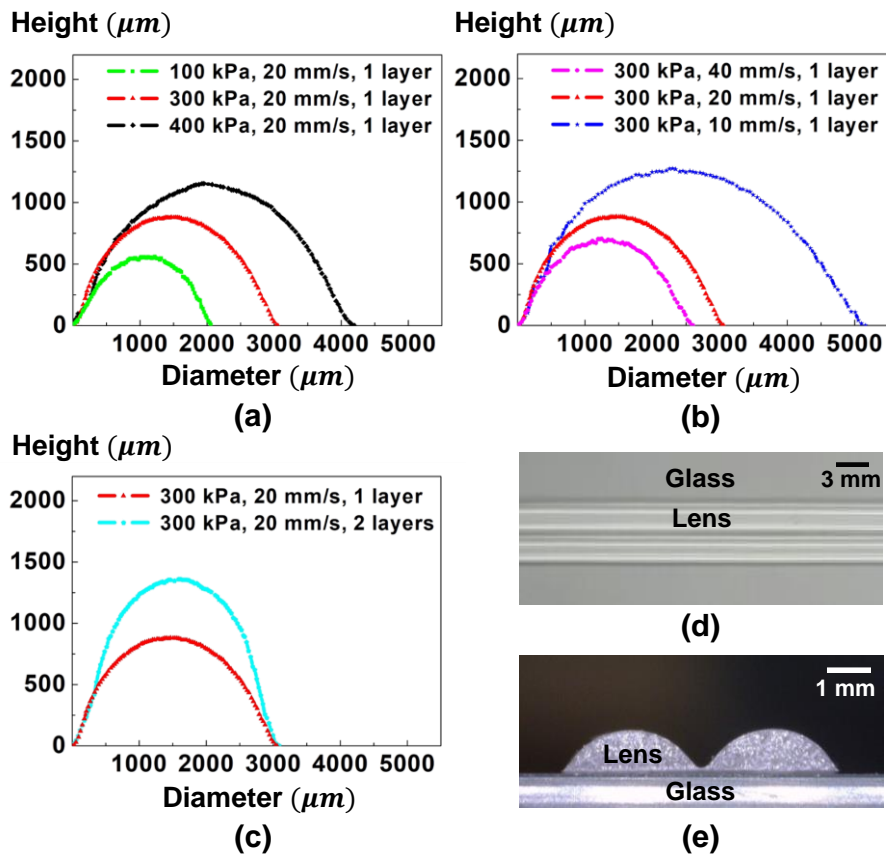
Figure 2.6. Cross-sectional profiles of the cylindrical lens with different (a) jetting pressure, (b) moving speed of stage, and (c) number of stacked layer. Camera images of the CLP from the (d) top and (e) cross-section view [26].

cylindrical lens is measured. It is observed that each cylindrical lens shows an aspherical cross-section. The diameter of the cylindrical lens increase as the stage speed decreased or jetting pressure increase. When NOA 63 is stacked by dispensing it again just above the partially cured cylindrical lens, the contact angle of the cylindrical lens increases while maintaining the diameter of the cylindrical lens. This means that the numerical aperture can be also adjusted through the stacking lens materials. Figure 2.6 (d) and (e) represent camera images of the CLP with a diameter of 3.058 mm, which is achieved by the moving speed of stage for 20 mm/s under the jetting pressure of 300 kPa without stacked layer. This result shows that each cylindrical lens is almost the same size and well-arranged without being merged.

To optimize the physical and optical parameters of CLP for seamless modular display system, the following optimization conditions are established: (1) Magnification with absolute value less than 2 (minimizing image distortion), (2) Viewing angle over 20°, and (3) glass thickness from 1 mm to 3 mm (the range of commercially available glass thickness). The calculated viewing angle and the magnification are plotted according to the changes of f-number and the thickness of glass under the condition that the seam width is 0.5 mm, as shown in Fig. 2.7. The results show that the viewing angle increase as the f-number decrease or the thickness of glass increase, as expected from Eq. (2.4). Based on the optimization conditions and the results shown in Fig. 2.7, the lens formed under the dispensing conditions with the moving speed of stage for 20 mm/s under the jetting pressure of 300 kPa without stacked layer, and the glass with 2.1 mm thickness are selected for implementing the seamless modular display. The calculation results for the optimized lens are denoted as red triangle (non-inverted shape) symbols.
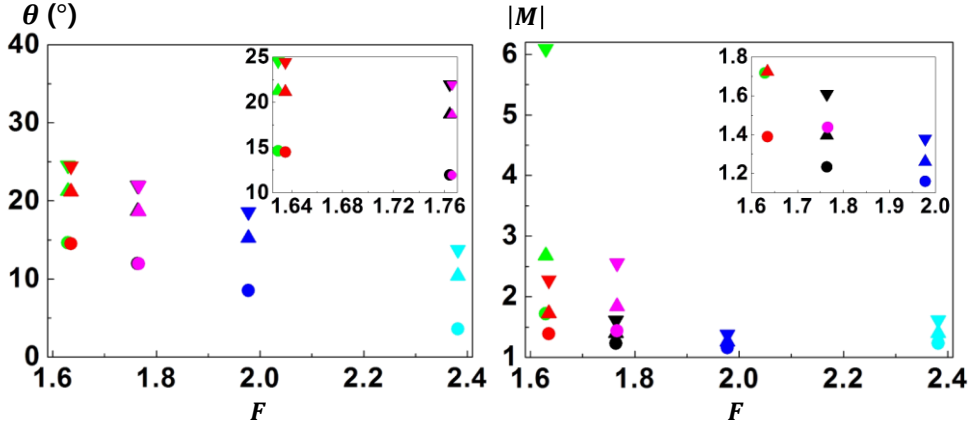
Figure 2.7. Calculation results of viewing angle (θ) and magnification ($|M|$) with *f*-number (F) of the cylindrical lens and the thickness of glass (t). The insets are magnified graphs showing detailed data [26].

Generally, the luminance is suitable criterion to quantify seamlessness [26, 53]. Since the seamless area is relatively brighter than the seam area, there is a luminance difference between the two areas, so that the optical concealment effect by CLP can be investigated by the luminance distribution. Figure 2.8 (a) is the 3D optical modeling of the LED backlight with CLP for ray-tracing simulation. The center of the seam is set as the origin of the position. The simulated optical system consists of the light-emitting part, seam, glass, and CLP with the optimized variables ($F = 1.635$, $|M| = 1.724$, $t = 2.1$ mm, $2s = 0.5$ mm). As a result, in the case of simulation, the variation of luminance is reduced from ±49.76 % without CLP to ±1.75 % with CLP, as shown in Fig. 2.8 (b). To verify simulation results, the luminance distribution of backlight with CLP and those without CLP are measured. As a result, in case of
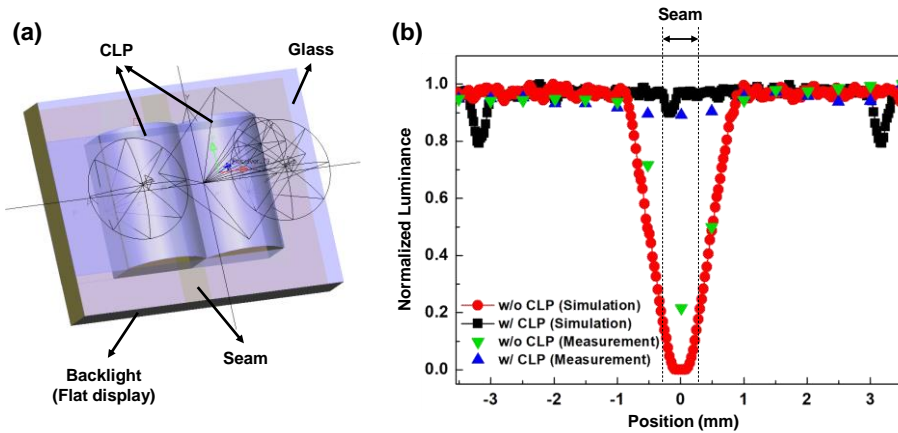
Figure 2.8. (a) 3D optical modeling for ray-tracing simulation. (b) Comparison of the luminance simulation and measurement results of the LED backlight without and with the optimized CLP [26].

the measurement, As a result, in case of the measurement, the variation of luminance is reduced from ± 39.23 % without CLP to ± 5.44 % with CLP, as shown in Fig. 2.8 (b). The uniformity of the measured luminance at the same position is higher than 96 %. From both simulation and measurement results, It can be concluded that the luminance is uniformly distributed by adding CLP onto the seam. According to Fig. 2.8 (b), the luminance of the optical system at the vicinity of the CLP boundary (Position = ± 3 mm) is reduced by about 20 % compared to that inside of CLP in the case of the simulation. This is because a part of the incident light on the top of the cylindrical lens surface at the boundary region cannot escape into the air by total reflection [54]. As a result, the luminance is not uniformly distributed and the boundary of CLP appears as a bright stripe. To solve this effect, it is possible to consider the method for optimizing the light energy distribution by using a freeform lens and diffuser [55].

By assigning the optimized design variables to the Eq. (2.1) and (2.2), which are used in the luminance simulation and measurement, viewing angle of the seamless display is calculated as 21.16°. To compare this value with the real case, the viewing angle characteristics of the seamless modular display are investigated for LED backlight and the actual image. Figure 2.9 shows a seamless modular display for LED backlight and actual image with different viewing directions. In the case of using LED backlight, the system configured previously for luminance measurement is used. As expected, the seam is not visible in the viewing range of -10° to +10° (total of 20°) and is still not recognized in the viewing range of -20° to +20° (total of 40°), which is beyond the theoretically expected viewing angle. If the total angular range is wider than 40°, the seam begins to be visible, resulting in a wider seam width than the actual seam width.

The reason why the seam is not visible at the larger viewing angle than the theoretical value is presumed to be the resolution limitation of the human eye or camera. The angular resolution of a human eye is known as about 1/60° [56] and that of a camera in case of capturing an actual image is about 1/58° which can be calculated from the pixel number of the image sensor in the horizontal direction (4920), the horizontal field of view (185 mm), the magnification (4) and the viewing distance (500 mm) [57]. If the angular resolution is converted to the distance resolution, it is 145.44 µm for the human eye and 150.40 µm for the camera. Due to this limitation, the seam can be unrecognizable to the observer even though the observation angle is larger than the theoretical viewing angle until it reaches the angular or distance resolution of the observer depending on the viewing conditions, according to the psychophysical requirement for modular display [58].
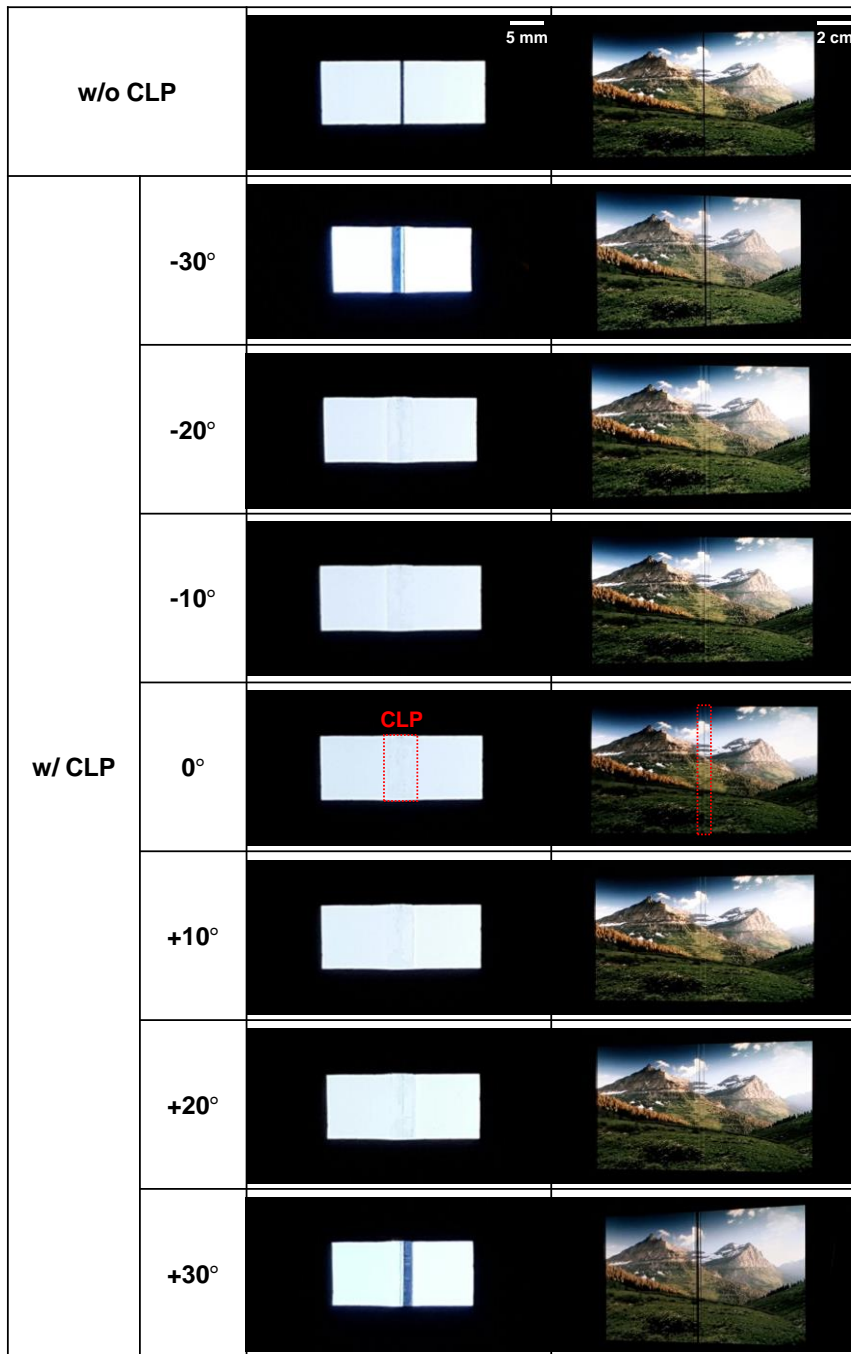
Figure 2.9. Seamless modular flat display from different views. A positive sign (+) of the angles denotes clockwise rotation, and the opposite direction is represented as a negative sign (-) of the angles viewed from the front of the image [26].

2.3. Seamless Modular Curved-edge Display with Printed Mirror

2.3.1. Main Concept

Figure 2.10 represents an imaging system involving a concave mirror in a seamless modular curved-edge display. The projection image generated by the reflection of the image at the curved-edge area from the concave mirror should be inverted so that observers see the continuous image from the front view. The reflected image covers the seam, thereby leading to an optical seam concealment effect. The cross-sectional profile of the concave mirror is designed as a conic curve to simplify parametric modeling.
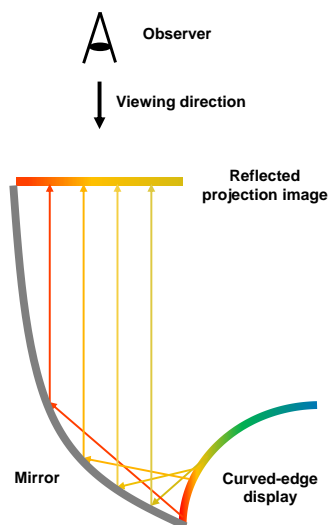
Figure 2.10. Image-forming behavior of concave mirror and principle of seamlessness appearance due to the reflective projection image of the object generated by a concave mirror.

2.3.2. Experimental Section

For parametric curve modeling of the cross-sectional profile the concave mirror, the rational Bézire conic curve [59] is adopted, which is widely used in CAD. The weight value is controlled to vary the structure of the concave mirror. The stereolithography (STL) file of the designed concave mirror mold is generated with CAD software (Fusion 360, Autodesk) and transferred to an FDM-type 3D printer (DP200, Sindoh). PLA is selected as a printing material for concave mirror molds and is the most widely commercialized material in the 3D printing industry due to its eco-friendliness and low-cost characteristics [60]. Figure 2.11 shows the fabrication process of a concave mirror with a 3D printed mold. A PLA plastic mold with 100 μm resolution (thickness of 1 layer) is fabricated and firmly attached to a glass substrate with an acrylic form (VHB^{TM} tape, 3M). The PDMS base and curing agent (Sylgard 184, Dow Corning) are mixed at a weight ratio of 10:1 by a centrifugal paste mixer (ARE-310, Thinky) and pouring it into a concave mirror mold. The reason for the choice of PDMS is that it is easy to separate from the PLA mold [61], so the desired structure can be replicated well. Air bubbles that are generated during pouring are removed in a vacuum desiccator for approximately 1 hour. After thermal curing at 120 ℃ of 30 min, the PDMS replica is detached from the concave mirror mold. For surface planarization of the PDMS replica, a mixture of the PDMS base and curing agent with the same weight ratio as the PDMS replica is coated by spin coater (SPIN-1200D, Midas System) at 1200 rpm for 60 s. After that, the surface planarized PDMS replica is thermally cured again at 120 ℃ of 30 min and then treated with UV cleaner (AH-1700, Ahtech LTS) at 184 nm/254 nm wavelength and
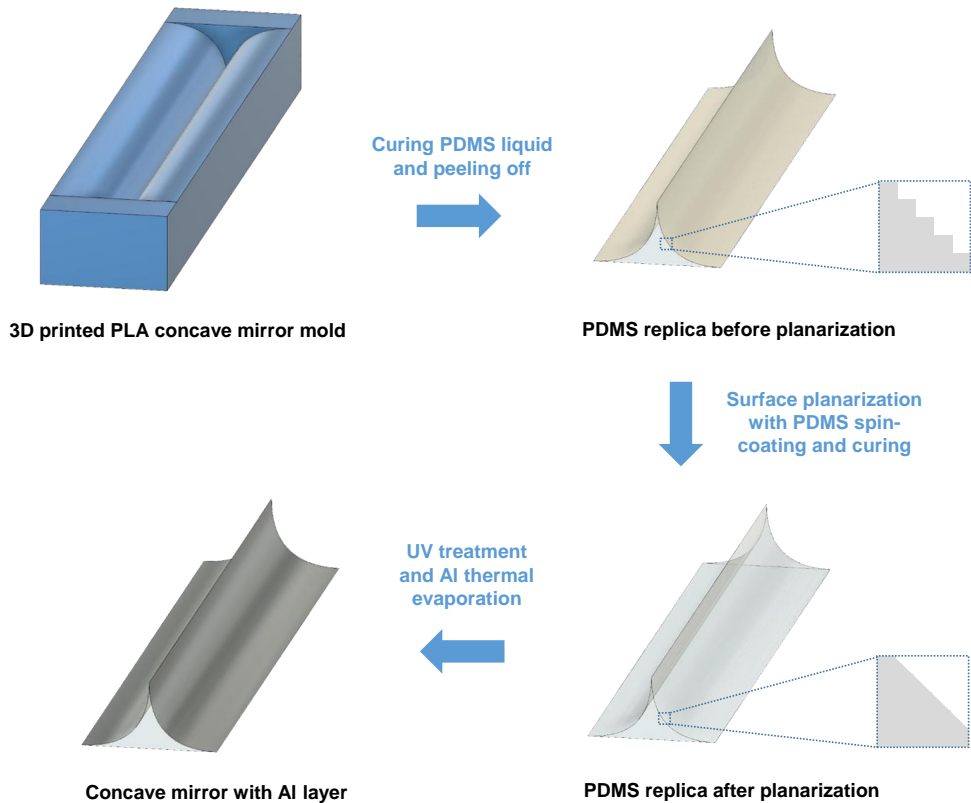
Figure 2.11. Fabrication process of a concave mirror with 3D printed mold. The insets show cross-sectional images of PDMS replicas before and after surface planarization.

30 mW/cm^2 intensity for 30 min to form a silica-like layer. Finally, an Al layer of 50 nm thickness is deposited with a customized vacuum thermal evaporator (Woosung Hi-vac) under 10^{-5} torr, thereby completing the fabrication of the concave mirror.

The total reflectance (R_T) and the diffuse reflectance (R_D) of the Al layers are measured by a spectrophotometer (CM-5, Konica Minolta) in the range from 360 nm to 740 nm with 10 nm interval, and the specular reflectance (R_S) is calculated by subtracting the R_D from the R_T. The cross-sectional views of PDMS replicas are

observed with an optical microscope (OM, DSX510, Olympus) in bright field mode. The surface morphology images of the Al layer in top view are captured with a field emission scanning electron microscope (FE-SEM, S-4800, Hitachi). The surface roughness of the Al layer is measured by atomic force microscope (AFM, XE-100, Park System) in noncontact mode. The luminance distribution is analyzed with ray-tracing simulation software (LightTools 8.5, Synopsys) and measured along the modular curved-edge display under the white image in the horizontal direction by using a luminance meter (CS-200, Konica Minolta) at a distance of 500 mm and an aperture of 0.1°. A Galaxy Note Edge (SM-N915S, Samsung Electronics) is selected as a curved-edge display product to demonstrate the seamless modular display.

2.3.3. Results and Discussion

In general, surface planarization is conducted to fabricate optical components with 3D printing because their surface roughness should be on the order of tens of nanometers, which is much lower than that of a typical 3D printed structure with a scale of tens of micrometers. Methods for surface planarization have been developed, such as femtosecond laser smoothing [62] and meniscus equilibrium process [63]. However, femtosecond laser equipment is expensive, and it is difficult to precisely control the experimental conditions in the meniscus equilibrium process. Unlike these two processes, spin coating of additional viscous liquid has the advantage of enabling surface planarization by merely adjusting the coating speed and time. Depending on the spin coating speed, the thickness of the coated layer varies, as shown in Fig. 2.12. It can be confirmed that surface planarization is completed under a certain spin coating speed. In Fig. 2.13 (a) and (b), cross-sectional views of the PDMS replica are shown before and after surface planarization. Before surface planarization, the surface of the PDMS replica protrudes because the surface of the 3D printed PLA mold protrudes. By spin coating additional PDMS liquid, the surface of the PDMS replica is flattened. The insets are the PDMS replica before and after surface planarization on the number '1'. Before surface planarization, the number appears blurry. However, it is clearly visible after surface planarization, indicating that the surface of the PDMS replica has been flattened. Figure 2.13 (c) and (d) display oblique and cross-sectional views of the fabricated concave mirror, respectively. The Al layer shows a noticeably reflected surface without perceptible lines of the 3D printed structure due to the smooth surface of the PDMS replica.
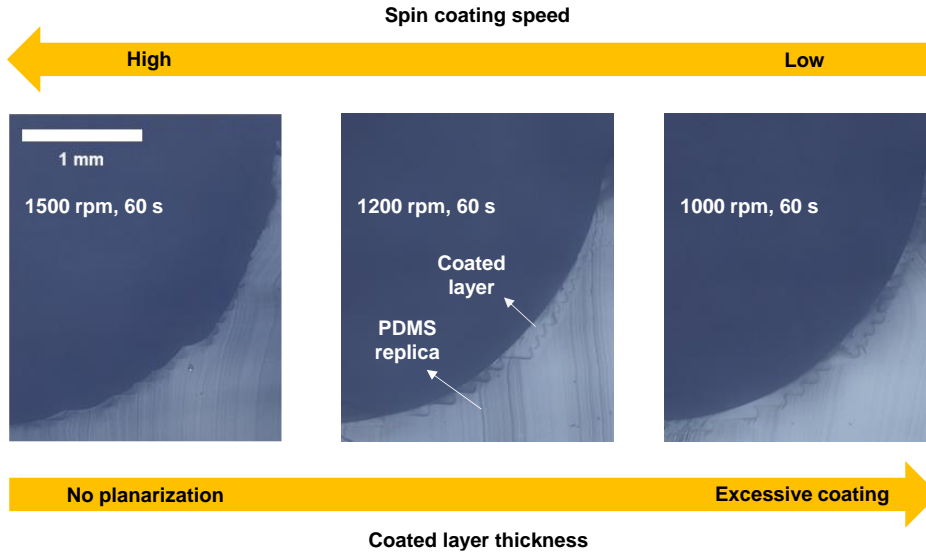
Figure 2.12. Relationship between spin coating speed and coated layer thickness of additional PDMS liquid.
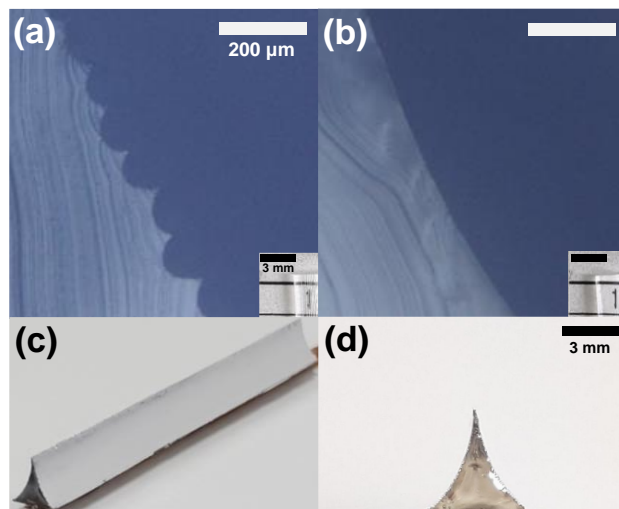
Figure 2.13. OM images from the cross-sectional view of the PDMS replica (a) before and (b) after surface planarization. The insets show the PDMS replica on the number '1'. Camera images of the concave mirror from the (c) oblique and (d) cross-sectional view.

The R_T and R_D of Al layers deposited on glass, bare PDMS, and UV-treated PDMS substrates are presented in Fig. 2.14 (a) and (b). The reason for measuring the R_D is to determine the clarity of the reflected image. Generally, the R_D increases as the surface roughness increases [64]. When the metal layer is fabricated by thermal evaporation directly on the PDMS without any surface treatment, a wrinkled structure is formed due to thermal expansion of the PDMS surface by local heating and cooling to room temperature after finishing the process [65]. As a result, diffuse reflection occurs, showing a hazy reflected image. However, when UV treatment is applied to the PDMS surface, the thermal expansion of the PDMS is reduced due to the rigidity of the silica-like layer formed by UV light [66], thereby suppressing the formation of wrinkles. The surface roughness of the UV-treated PDMS surface is lowered so that a clear reflected image can be observed withe the well-formed mirror layer. In the case of the glass, the Al layer exhibits an R_T of 91.97 %, R_S of 90.99 %, and R_D of 0.98 % at a 550 nm wavelength. The Al layer on bare PDMS has an R_T of 23.89 %, R_S of 1.06 %, and R_D of 22.83 % at the same wavelength. However, the Al layer on UV-treated PDMS shows an R_T of 91.87 %, R_S of 90.84 %, and R_D of 1.03 %, comparable to the Al layer results for glass. In general, a reflected image without visual loss is observed when R_S is higher than 80 % [67]. This means that the Al layer on UV-treated PDMS can function as a mirror in seamless modular display systems.

Figure 2.14 (c)-(e) show the surface morphology of the Al layer on glass, bare PDMS, and UV-treated PDMS, respectively. In the top view of SEM images, randomly formed wrinkles are observed in the Al layer on bare PDMS (Figure 2.14 (d)), while there are no wrinkles in Al layer on glass (Figure 2.14 (c)) and UV-treated PDMS (Figure 2.14 (e)). The surface roughness of each sample is also examined by

AFM. Typically, the appropriate surface roughness range for optical components is lower than one-tenth of the visible light wavelength region (< 40 nm) [68]. The surface roughness of the Al layer on bare PDMS is measured to be 63.782 nm root-mean-square (RMS) (Figure 2.14 (g)), while that of Al layer on UV-treated PDMS decreases to 5.066 nm RMS (Figure 2.14 (h)), which is comparable to that of the Al layer on glass, with a value of 1.366 nm RMS (Figure 2.14 (f)). This indicates the suppression of wrinkles by UV treatment of the PDMS surface, and the Al layer on UV-treated PDMS satisfies the roughness requirement for utilization as a mirror.

To find the concave mirror structure that displays a continuous image in the modular curved-edge display, a concave mirror with a width of 5.14 mm is placed on the seam formed by attaching two commercialized curved-edge display panels. Figure 2.15 (a) and (b) show a comparison of the light path according to the concave mirror structure. In Fig. 2.15 (a), the reflective projection image cannot cover the area near the boundary of the curved-edge display and the concave mirror. As a result, the seam is still observed in front of the modular curved-edge display. Therefore, it is necessary to find a concave mirror structure to expand the reflective projection image to enhance the seam concealment effect, as shown in Fig. 2.15 (b). The curved-edge display used in the experiment has an edge width (W_{edge}) of 7.03 mm and an edge height (h_{edge}) of 3.05 mm, and the edge curve is fitted with a parabola.

To investigate the image continuity obtained concave mirror structures, four kinds of concave mirrors are prepared, and their structural parameters are presented in Table 2.1. To quantify the image continuity, the FF is defined as the ratio of the reflected projection image area to the seam area from the front view. In Fig. 2.16 (a), black lines are shown near the area where the curved-edge displays meet Mirror #1
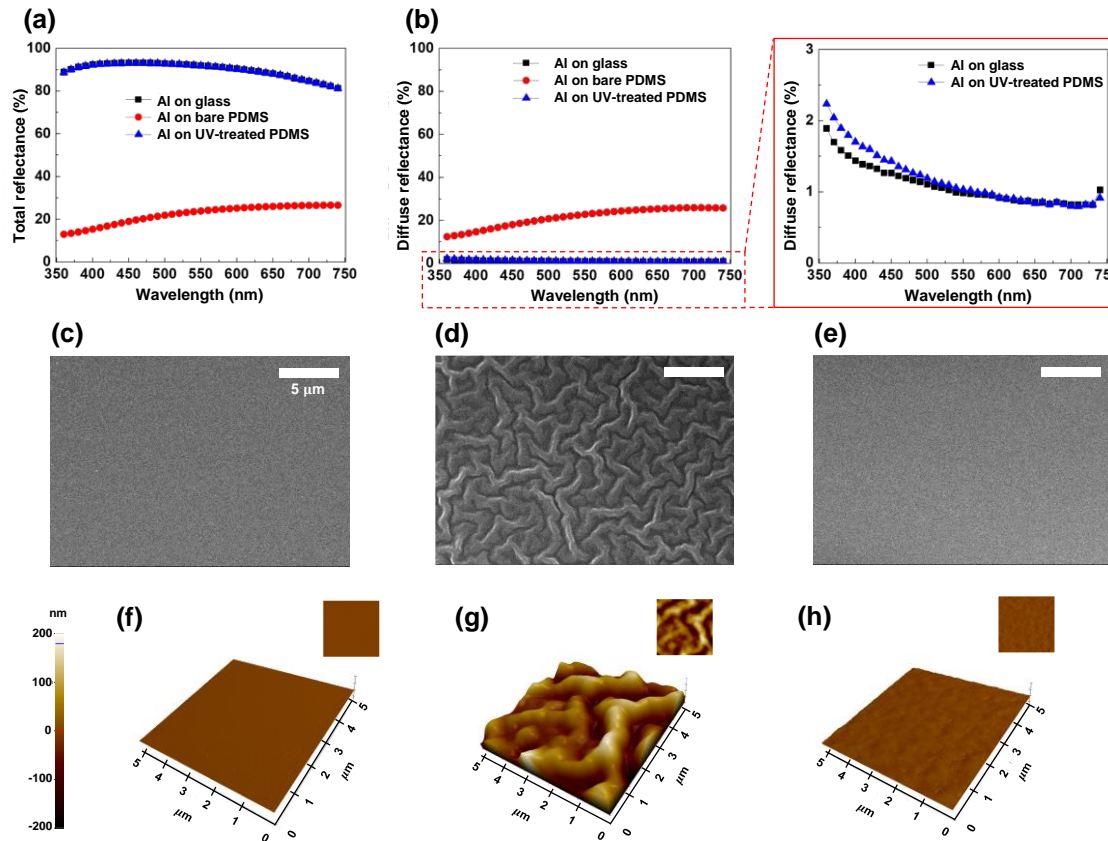
Figure 2.14. (a) Total reflectance and (b) diffuse reflectance of the Al layer on glass, bare PDMS, and UV-treated PDMS. SEM images of the Al layer on (c) glass, (d) bare PDMS, and (e) UV-treated PDMS. AFM images of the Al layer on (f) glass, (g) bare PDMS, and (h) UV-treated PDMS.
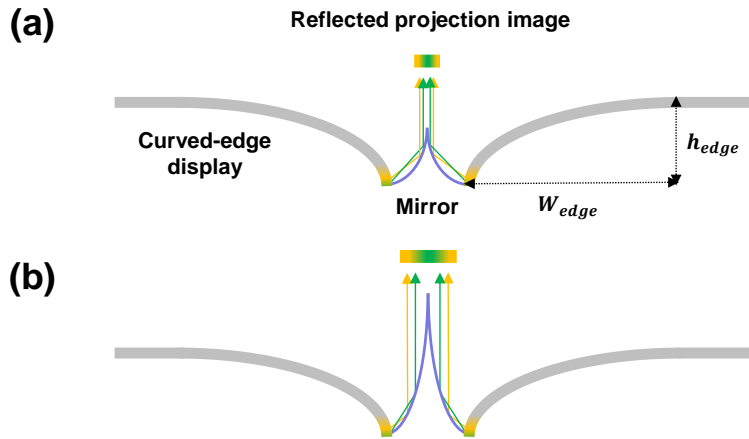
Figure 2.15. Comparison of the light path from the image near the boundary of the curved-edge display and concave mirror when showing reflected projection images with (a) small and (b) large sizes according to the concave mirror structure. The emission point and direction of the ray are assumed to be the same for (a) and (b).

	Width (mm)	Height (mm)	Weight	Type of curve
Mirror #1		2.80	1.00	Parabola
Mirror #2	5.14	3.82	1.00	Parabola
Mirror #3		4.13	1.22	Hyperbola
Mirror #4		5.22	0.67	Ellipse

Table 2.1. Cross-sectional geometric parameters of concave mirrors for investigating image continuity of the modular curved-edge display. The weight is defined in Ref. [59].

because the mirror only reflects part of the light emitted from the images on the curved-edge display, and the FF is 41.9 %. Although the black lines are still observed in the case of both Mirror #2 and #3, portions of the reflected image on the seam area are increased to 48.4 % and 58.1 %, respectively. Finally, a seamless modular image
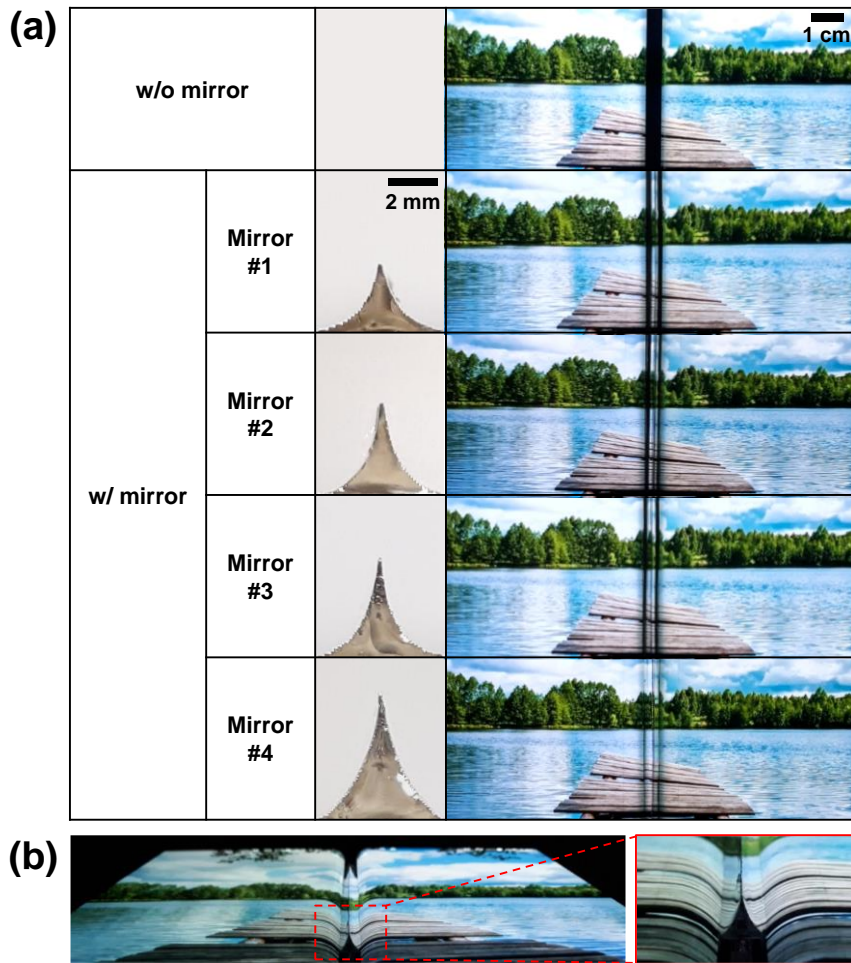
Figure 2.16. (a) Variation in the image continuity of the modular curved-edge display according to the concave mirror structure. (b) Oblique view of the seamless modular image.

is demonstrated with Mirror #4, and the widths of the black lines are reduced significantly, thereby representing an FF of approximately 100 %. The oblique view of the seamless modular image is shown in Fig. 2.16 (b).

After determining the concave mirror structure for the seamless modular curved- edge display, the luminance distributions of the modular image without and
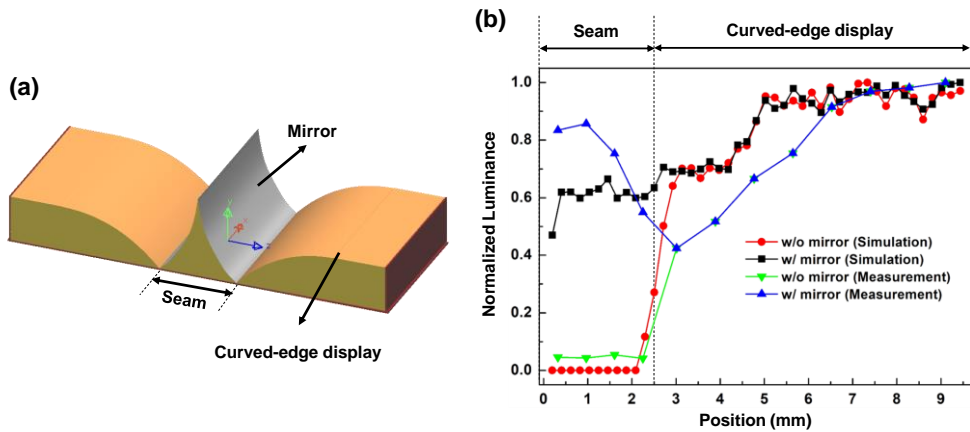
Figure 2.17. (a) 3D optical modeling for ray-tracing simulation. (b) Comparison of the luminance simulation and measurement results of a modular curved-edge display without and with a concave mirror. The adopted concave mirror is Mirror #4.

with the concave mirror are simulated and measured from the front view. According to previous studies related to seamless modular displays, the luminance distribution is the proper criterion to evaluate seamlessness, as explained in chapter 2.2.3. Figure 2.17 (a) shows the 3D optical modeling of the modular curved-edge display with the concave mirror for ray-tracing simulation. The center of the seam is set as the origin of the position. The average luminance in the seam area is increased from 3.23 % to 60.63 % in the simulation and from 4.62 % to 74.85 % according to measurement results by placing the concave mirror onto the seam, which verifies the seamlessness of the modular curved-edge display, as shown in Fig. 2.17 (b). There is a difference in luminance in the seam area before and after placing the concave mirror, which means that the seam concealment effect is due to the concave mirror. Since the luminance is measured from the front view, this results confirms hat the luminance of the curved-edge display decreases as the slope of the edge increases.

The viewing angle of the seamless modular curved-edge display is also investigated. As described in chapter 2.2.1, the viewing angle of a seamless modular display is defined as the maximum angular range at which seam is not visible from the observer's view point. Although the reflected image becomes darker when the observation position is outside the front, the seam is not visible in the viewing range from -30° to +30° (total of 60°), as shown in Fig. 2.18. It is presumed that the viewing range is limited because the areas that cannot be covered by the reflected image appear near the boundary of the concave mirror and the curved-edge display and the uncovered areas are enlarged from a certain viewing angle or more, thereby being observed as a black image.

Due to the limited resolution of 3D printers, the width of the concave mirror apex is the minimum feature length of a 3D printed structure, and its value is approximately 100 μm, as shown in Fig. 2.19. According to previous research related to human vision, the angular resolution of a typical human eye is approximately 1/60°, as mentioned in chapter 2.2.3. If the angular resolution is converted to distance resolution, the viewing distance for resolving a length of 100 μm is calculated to be 344.8 mm. In general, the viewing distance of small- and medium-sized displays is approximately 300 mm [69]. Therefore, the concave mirror apex can be recognized by the observer because the viewing distance is shorter than 344.8 mm. It is expected that the concave mirror apex will be imperceptible for the observer if it has a narrow width obtained by using a high-resolution 3D printer with a scale of tens of micrometers.

Front view (0°)

(Counter-clockwise rotation)

(Clockwise rotation)

1 cm

-10°

+10°

-20°

+20°

-30°

+30°

-40°

+40°
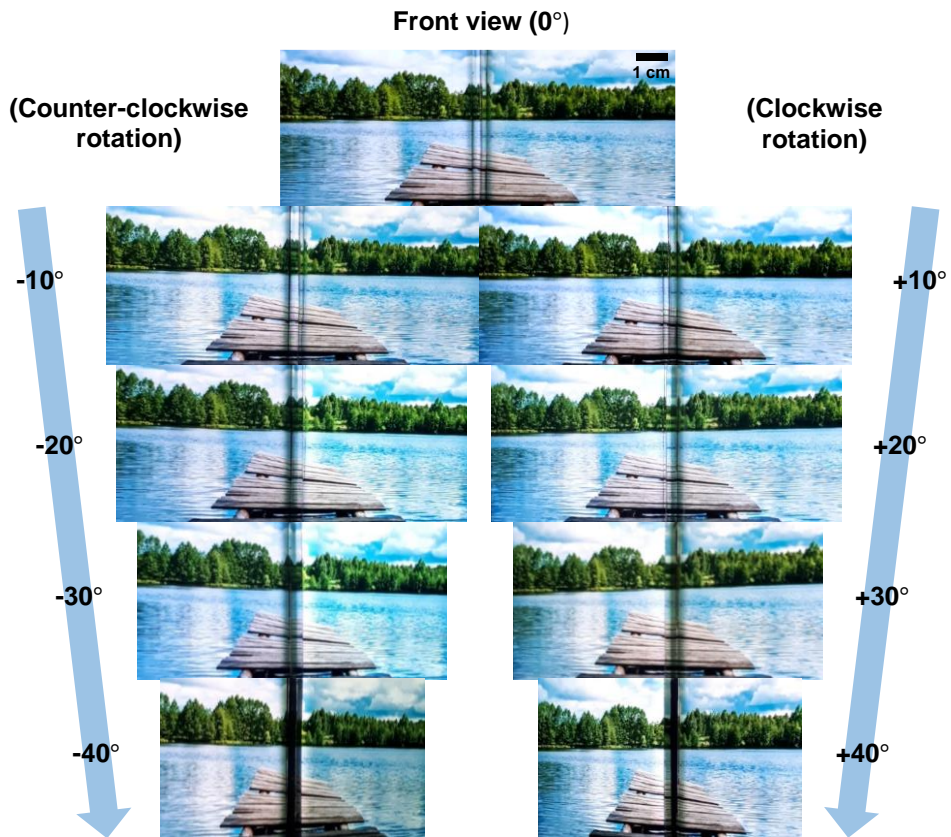
Figure 2.18. Seamless modular curved-edge display from different views. A positive sign (+) of the angles denotes clockwise rotation, and the opposite direction is represented as a negative sign (-) of the angles viewed from the front of the image.

3 mm

200 μm

~ 100 μm

Apex of mirror
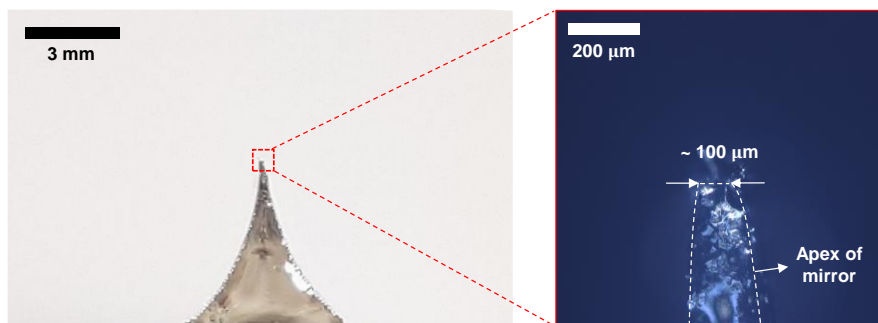
Figure 2.19. Cross-sectional images of the concave mirror (Mirror #4) and its apex.

2.4. Conclusion

To summarize, previous reports about the seamless modular display and macro-scale printed lens and mirror are briefly introduced in chapter 2.1. In chapter 2.2, a facile method for implementing a seamless modular flat display simply by forming CLP is proposed. The CLP is fabricated by dispensing optically transparent UV curable adhesive with adjusted jetting conditions. Based on the optimized design parameters, the effect of CLP for obtaining seamlessness characteristic is verified through ray-tracing simulation and measurement of luminance distribution. Finally, a seamless modular flat display is demonstrated with CLP, resulting in a viewing angle of the seam concealment of 40°. Besides, a seamless modular curved-edge display with a concave mirror which is designed and fabricated with 3D printed plastic mold is suggested in chapter 2.3. The concave mirror is placed on the seam of modular curved-edge displays to remove image discontinuity by reflecting images at the curved-edge region toward the observer direction. By modifying the height and curvature of the concave mirror based on geometric optics and parametric modeling of the profile, a continuous image of modular curved-edge displays is observed. The luminance distribution of seamless modular curved-edge displays is measured to verify the seam concealment effect with 60° viewing angle.

Through the work investigated in this chapter, it is verified that the 3D printed optical components can be utilized potentially in the display industry. It is expected that establishing a seamless modular display will pave way for the realization of various forms of screen devices via a straightforward and cost-effective method.

Chapter 3

Micro-scale Printed Optical Components

3.1. Introduction

This chapter introduces a printed color-convertible lens in the micro-scale and its applications to a full-color micro-LED array. The applications of micro-scale optical components in displays are suitable for internal devices such as microlens and color filter on LCD, OLED, and micro-LED, as discussed in chapter 1.3. However, most of the microlens and color filter have been applied to many products in the case of LCD and OLED. Recently, micro-LED is attracting much attention for next-generation display technology since it has many advantages over LCD and OLED in terms of performance such as low energy consumption, high pixel density, high brightness, long lifetime, and short response time [70]. Due to these merits, micro-LED can be utilized in various applications including argument reality (AR) [71] and visible light communication [72] devices. Accordingly, the application of microlens [73] and color filter [74] to micro-LED has been still investigated for highly efficient and full-color micro-LED displays.

For the demonstration of a full-color micro-LED array, there are two main approaches: Fabricating red (R)/green (G)/blue (B) micro-LED separately and

depositing R/G color converter on blue micro-LEDs. Since it is almost impossible to simultaneously grow an active layer emitting R/G/B colors on a single wafer, a pick-and-place method such as utilizing elastomeric stamp [75] and assembly by programmable electric field [76] for separating each color chips should be required to construct a full-color micro-LED array. However, millions of micro-LED transfer by pick-and-place method is impractical for manufacturing products due to a long process time. Also, images cannot be presented properly as time goes by from different degradation rates of each color of the micro-LED.

To overcome the difficulty in implementing monolithic and full-color micro-LED arrays, an approach to fabricate monochromatic micro-LED arrays such as UV or blue light and then deposit down-converting materials on micro-LED selectively to be used as a color conversion layer. For achieving this approach, two things should be considered. The first thing is the selection of the color converting materials. There are several candidates of color converting materials such as organic dye [77], phosphor [78], and QD [79]. Organic dye has been for a long time in human history and is traditionally used for clothes and food. In modern technology, it has been generally adopted for molecular labeling in bioengineering. However, it is difficult to use as a color conversion material for micro-LED due to its low thermal stability and color bleaching. Phosphor is the most widely used color-converting material for the LED industry because of its excellent luminous efficiency, stability, and low-cost. On the other hand, there is a disadvantage that it is difficult to be applied to micro-LEDs because the phosphor particle size is several to tens of micrometers. Recently, QD has emerged as a key material for a light source and color filter in next-generation display devices like quantum dot light-emitting diodes (QLEDs). It

exhibits superior characteristics for LED applications such as broad absorption range, wide color gamut, and color purity. It is a suitable material for color conversion because it is simple to tune the wavelength of emitted light according to its diameter. However, to use the QD layer as a color converter, the thickness should be several micrometers or more for increasing absorption of light within QD by extending light-path length according to the following equation [80,81]:

$$A = 1 - e^{-\alpha d} \tag{3.1}$$

where A is the absorption ratio of light, α is the QD absorption coefficient of light, and d is the light-path length in the QD layer. So there have been several reports to secure sufficient thickness of QD by mixing polymer matrix with high viscosity to form a QD/polymer composite [82,83]. A technique that allows QD to be well dispersed without aggregation in the polymer matrix is critical during the mixing of the QD and polymer for preserving quantum yield and photostability. When QD aggregation occurs in QD/polymer composite, the optical properties are degraded due to excessive optical scattering losses. For this reason, several studies are being conducted to increase the compatibility between QD and polymer matrix [84].

Until now, Cd-based synthesized QD has been mainly commercialized [85]. However, the need for eco-friendly materials-based QD has increased due to environmental problems and the restriction of hazardous substances (RoHS) in the electronics industry [86], and indium phosphide (InP)-based QD is an example of non-Cd-based QD [87, 88]. Although InP-based QD has a still problem of low quantum efficiency, researches have been conducted such as the development of highly efficient InP-based QLEDs [89] and improving quantum efficiency by adding elements like gallium (Ga) [90]. Furthermore, application to LCD color filters has

also been reported [91]. In this chapter, InP/zinc selenium sulfide (ZnSeS)/zinc sulfide (ZnS) QD where InP is a core, ZnSeS acts as a buffer layer, and ZnS is a shell structure s adopted as the color converting materials.

The second thing is the patterning method of color converting materials. In general, a phosphor is dispensed on an LED chip for color conversion, but fine patterning by printing is difficult due to its size with tens of micrometers. QD is in the form of a colloidal ink and has a nanometer diameter, so it is suitable for fine printing. The color conversion layer or emitting layer with QD can be formed by applying various printing methods such as piezoelectric [92] and aerosol jet printing [79]. However, as the solvent evaporates, the thickness uniformity of the printed QD layer is low due to the coffee ring effect. For this reason, a method for patterning the QD/polymer composite has been reported as mentioned above. A representative method for patterning QD/polymer composite is to utilize the photolithography process [93]. The photolithography is conducted by using QD/photoresist composite, and there is an advantage that an established method is used. But the photolithography is a kind of subtractive manufacturing and one step of the conventional semiconductor fabrication process, it has demerits that expensive maintenance is required and heavy waste of material is involved.

For this reason, a method for patterning high-viscosity materials like QD/polymer composite accurately by printing is considered, and EHD printing appears to be suitable for facile application of fine patterning to micro-LEDs. EHD printing is a method of finely jetting a functional liquid by applying a high electric field between the nozzle and target position [10]. Advantageously, the desired pattern can be obtained without a mask in a range of several micrometers. Due to this

advantage, much research has been reported related to applications of EHD printing to high-resolution devices such as a thin-film transistor (TFT) [94], OLED [95], QLED [96], and optical components [97]. In EHD printing, the electric force (F_e) can be formulated as the following equation [98]:

$$F_e = \rho_f E - \frac{1}{2} E^2 \nabla \varepsilon + \nabla \left(\frac{1}{2} \rho \frac{\delta \varepsilon}{\delta \rho} E^2 \right) \qquad (3.2)$$

where ρ_f is the free charge density in the liquid, E is the electric field, ε is the permittivity, and ρ is the density of the liquid. By optimizing the various printing parameters such as applied voltage, the height of nozzle, viscosity, and dielectric constant of materials, the meniscus is changed to flow of liquid with the shape of a cone, which is called Taylor cone, by overcoming a critical value of electric force [99]. Environmental conditions including temperature and humidity can also affect the electric force due to the change of free charge density or density of the liquid.

Combining these backgrounds, EHD printing of QD/photocurable polymer composite for the color filter with lens shape is reported in chapter 3.2. QD-embedded microlenses are fabricated with various sizes by adjusting EHD printing conditions and applied to blue micro-LED array for full-color micro-LED display applications.

3.2. Full-color Micro-LED Array with Printed Color-convertible Microlens

3.2.1. Main Concept

As mentioned in chapter 3.1, microlens and color filter are indispensable components of optoelectronic devices. To simplify the process steps of both components and reduce the thickness of the device, a structure called a 'lens-shaped color filter' is suggested. There are several applications to devices such as complementary metal-oxide-semiconductor (CMOS) image sensor [100], OLED [101,102], and optical microscope [103]. In general, color filter and microlens are located on photodiode in CMOS image sensor structure. By etching a color filter with lens shape, the lens-shaped color filter can be fabricated. As a result, the crosstalk is lower and the signal-to-noise ratio (SNR) is higher without changing color filter materials. In the case of OLED, a color-convertible outcoupling lens is adopted, thereby achieving high efficiency and color conversion simultaneously. For the application of lens/color filter combined system in a microscope, photonics crystal structure is embedded in PDMS macrolens, thereby integrating several optical characteristics such as light shaping, magnification, and color tuning. Previous studies as mentioned above select phosphors, organic dyes, or photonic crystals as color converting materials or structures, and utilize conventional semiconductor fabrication process. Recently, researches related to lens-shaped color filters with QD fabricated by printing method have been reported [104,105]. But there are still no cases of applying to micro-scale devices.
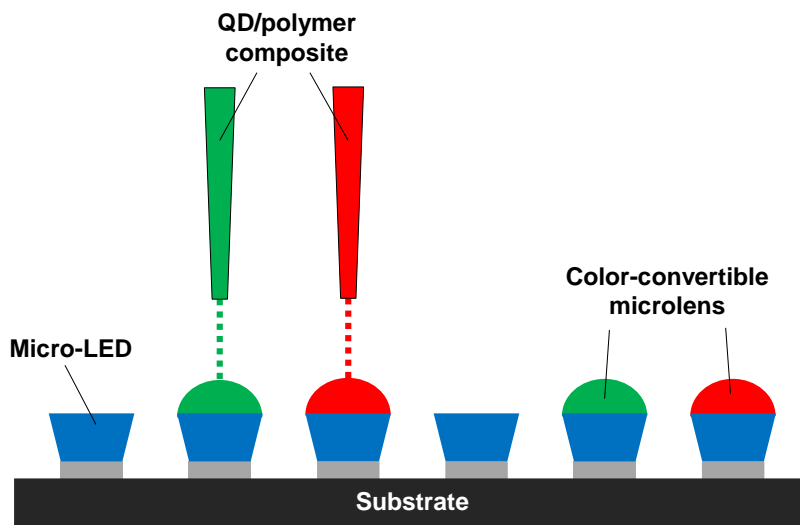
Figure 3.1. Schematic diagram of printed color-convertible microlens for full-color micro-LED array.

Inspired by these previous reports, a method of forming a lens-shaped color filter with EHD printing is proposed. When the QD/photocurable polymer is printed on a micro-LED, it becomes a hemispherical lens shape by the surface tension of the photocurable polymer. The fabrication of QD-embedded color-convertible microlens is completed by UV-curing, as shown in Fig. 3.1. Because of the self-maintaining property of the photocurable polymer, a bank structure that defines pixels is not required. Since the color-convertible microlens has a sufficient height of several tens of micrometers in a hemispherical shape, it is possible to act as a light extractor and color converter for a highly efficient, full-color micro-LED array.

3.2.2. Experimental Section

Figure 3.2 represents the preparation steps of the QD/photocurable polymer composite. Firstly, green/red InP/ZnSeS/ZnS QD solutions (solvent: toluene, ligand: oleic acid) are prepared. As a polymer matrix material, Norland Optical Adhesive 61 (NOA 61, Norland Products), which has been widely used as an UV curable liquid polymer, is selected due to its high transparency (~99 % at visible light wavelength), fast UV-curing property, and suitable viscosity (~300 cps) for the formation of hemispherical lens shape and stable EHD printing [106]. It also enables the encapsulation of QD and has good miscibility with the QD solution. The QD solutions and NOA 61 are diluted with toluene (Anhydrous, 99.8 %, Sigma Aldrich) to prevent aggregation of QD during the mixing. Diluted QD solutions and NOA 61 are mixed, followed by stirring until the boundary of each solution disappears. The mixed solution is placed in a vacuum chamber overnight to evaporate toluene, thereby completing the preparation of the QD/NOA 61 composite. Table 3.1 shows the QD concentrations of the QD/NOA 61 composite. The reason why the QD concentration when printing on micro-LED is higher than that when printing on glass is that after fabrication of the color-convertible microlens on the glass, it is irradiated with UV light with high absorption by QD to confirm the shape of the lens. However, since the micro-LED emits blue light with low absorption by QD, it is required to increase the QD concentration for efficient color conversion.

Before starting EHD printing of the QD/NOA 61 composite, surface treatments with oxygen plasma using a plasma system (CUTE, Femto Science) at 50 W for 1 min and trichloro(1H, 1H, 2H, 2H-perfluorooctyl)silane (FOTS) (97 % assay, Sigma
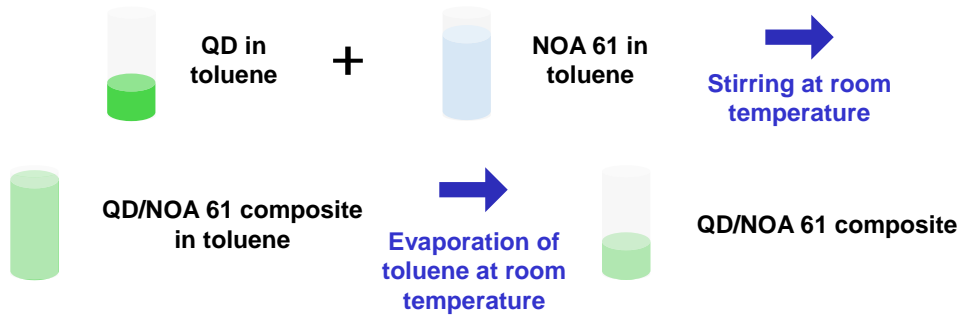
Figure 3.2. Preparation steps of the QD/polymer composite.

Printing target	QD concentration (mg/ml)	
	Green QD/NOA 61	Red QD/NOA 61
Glass	3.30	11.50
Micro-LED	9.25	22.50

Table 3.1. QD concentrations of the QD/polymer composite.

Aldrich), which is widely used for anti-adhesion surface treatment by forming a self-assembled monolayer (SAM) in molding process [107], for 30 min are conducted on the glass substrate or the blue GaN-based micro-LED array (LC Square) with 100 × 100 μm^2 area and 8 μm thickness for stable jetting of QD/NOA 61 composite. For EHD printing of QD/NOA 61 composite, it is injected into a metal-coated fine nozzle (SIJ-S30N, SIJ Technology) with a 30 μm inner diameter. The nozzle and the glass substrate or micro-LED array are placed on the stage of the EHD printer (SIJ-S050, SIJ Technology). After finishing EHD printing, QD/NOA 61 composite is cured immediately for 15 min with the 365 nm wavelength UV light having an intensity of 7 mW/cm^2 by using a portable UV lamp (LF206LS, UVITEC Cambridge). Photoluminescence (PL) images of EHD printed QD/NOA 61

composite on the glass substrate and micro-LED array are captured by optical microscope (DSX510, Olympus) in the dark field mode with UV light irradiation. The color-convertible microlens in oblique view is captured with a field emission scanning electron microscope (S-4800, Hitachi). The micro-LED with a color-convertible microlens is contacted with a metal electrode and its operation is carried out by applying voltage with probe station (MST-6000C, MS Tech), and down-converted light emissions from the blue micro-LED by the color-convertible microlens are captured by a camera included in the probe station. The normalized spectra and the 1931 Commission Internationale d'Eclairage (CIE) color coordinates of emitted light are measured by a spectroradiometer (CS-1000A, Konica Minolta).

3.2.3. Results and Discussion

Figure 3.3 shows the green/red InP/ZnSeS/ZnS QD/NOA61 composite and UV-cured droplet on the glass substrate. The QD mixed in the composite is well-dispersed without aggregation. If there are aggregated QDs, the composite appears turbid due to light scattering. In general, the QD concentration and PL intensity are a trade-off. If the QD concentration is lowered, the QD is likely to be well-dispersed and difficult to be aggregated in the polymer matrix, but the PL intensity is also lowered due to the small amount of the QD. Increasing the QD concentration can enhance the PL intensity, but the QD aggregation becomes severe when the QD concentration exceeds a certain range of values. Therefore, the optimization of QD concentration considering the trade-off relationship between the amount of QD and the PL intensity is an important factor when preparing the QD/polymer composite. The reason for mixing NOA 61 with QD solution after diluting with toluene is to maintain the well-dispersed environment of QD as much as possible even if it is mixed with NOA 61 since the QD is dispersed in toluene.

Another important factor in preparing QD/polymer composite is whether the solvent of QD has been removed. Because if UV light is irradiated for UV-curing on the composite with remained solvent, the solvent is evaporated by the energy of UV light, resulting in shape change and rough surface of UV-cured composite. To confirm this, a droplet of QD/NOA 61 composite from which the solvent is completely removed is placed on the glass substrate and solidified with UV light. It is observed that the QD/NOA 61 composite maintains its lens shape after completing UV-curing, as shown in Fig. 3.3.

Mixture (Before UV-curing)		Droplet (After UV-curing)	
Green QD/ NOA 61	Red QD /NOA 61	Green QD/ NOA 61	Red QD /NOA 61
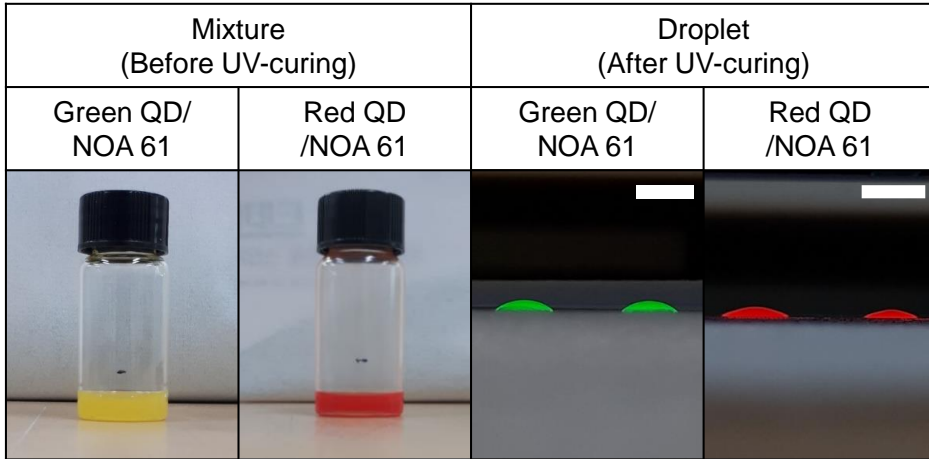
Figure 3.3. Camera images of the green/red QD/polymer composite and UV-cured droplet on the glass (scale bar: 5 mm).

To determine whether QD/NOA 61 composite can be printed, the jetting is performed on a glass substrate. It is confirmed that a shape of microlens array uniformly formed, as shown in Fig. 3.4, and the diameter of each lens can be adjusted according to the jetting condition such as jetting voltage, jetting time, the distance between the nozzle and the substrate, and nozzle diameter. Fig. 3.5 (a) and (b) show the diameters of color-convertible microlens presented in Fig. 3.4. When UV light is irradiated for capturing PL images, green and red appear in the microlens area, which means that the QD is embedded inside NOA 61. Before EHD printing, the glass substrate is treated with FOTS vapor to change its surface to hydrophobicity. This is because if the surface is not hydrophobic, the QD/NOA 61 composite spreads well due to the wetting characteristics, making it difficult to form a hemispherical lens shape. The diameters of the color- convertible microlens are all shorter than 100 μm, showing the possibility of being applied to micro-LEDs. Figure 3.6 shows the color-

	Lens array (Green) #1	Lens array (Green) #2	Lens array (Green) #3
w/o PL			
w/ PL			

	Lens array (Red) #1	Lens array (Red) #2	Lens array (Red) #3
w/o PL			
w/ PL			
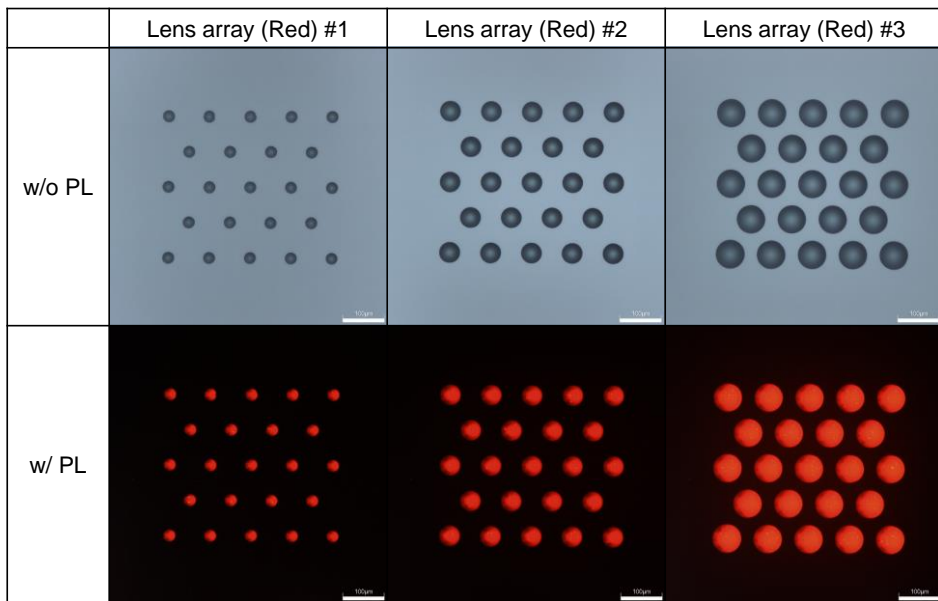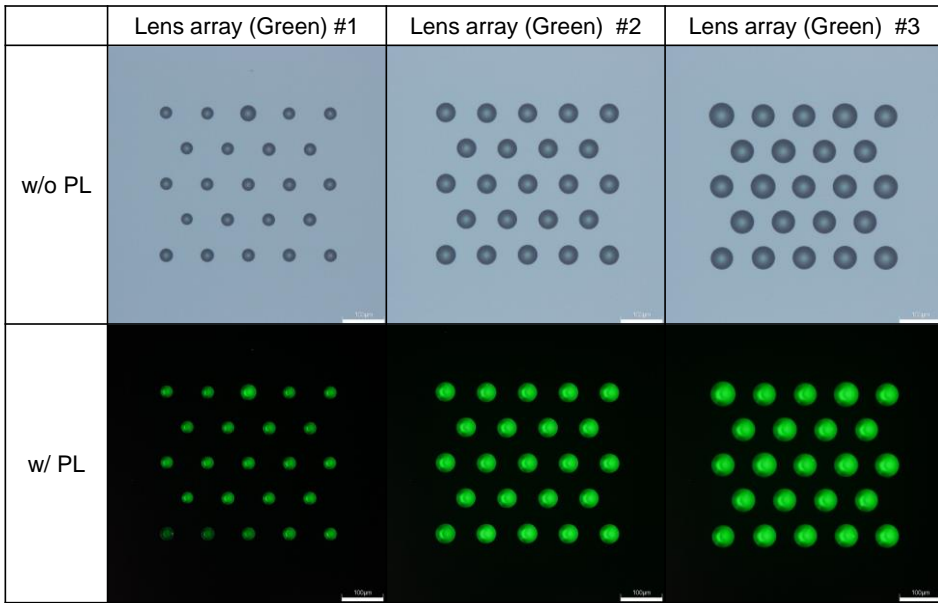
Figure 3.4. Photoluminescence images of the EHD printed green/red color-convertible microlens array with QD/polymer composite on the glass (scale bar: 100 μm).
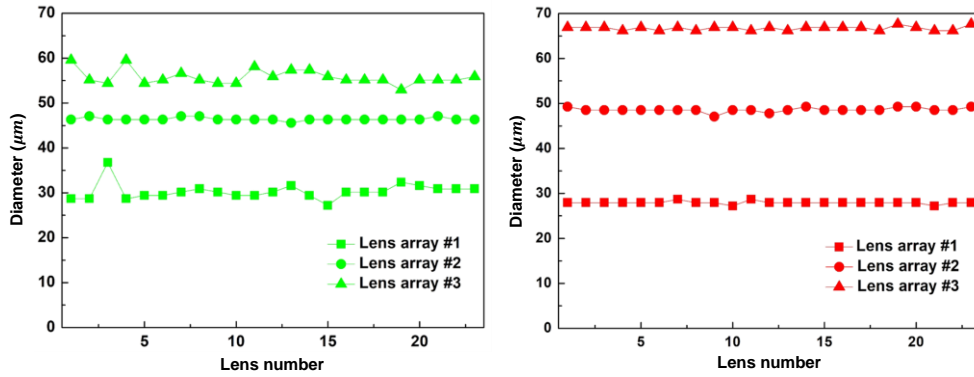
Figure 3.5. Measurement results of diameters of the EHD printed green/red color-convertible microlens array with QD/polymer composite on the glass presented in Fig 3.4.

convertible microlens array on the micro-LED array with $100 \times 100 \ \mu m^2$ square shapes, and it is also confirmed that the QD is embedded inside NOA 61 through the PL images.

Figure 3.7 shows the camera and SEM images of the color-convertible microlens placed on micro-LED from the oblique view. The micro-LED has a square shape with a side of 100 μm. The color-convertible microlens with a radius of about 50 μm is formed within the $100 \times 100 \ \mu m^2$ square regions of the micro-LED. From this observation, a sufficient thickness of QD/NOA 61 composite for a long optical path has been secured. The EHD printing of the QD/NOA 61 composite starts from the center of the micro-LED. The printed QD/NOA 61 composite maintains its shape of the hemispherical microlens during the jetting, and gets bigger, and then reaches the edge of the micro-LED. There is a step difference of about 8 μm between the micro-LED and the adjacent surface. The QD/NOA 61 composite does not flow toward the out of the micro-LED due to the pinning effect at the edge of the micro-
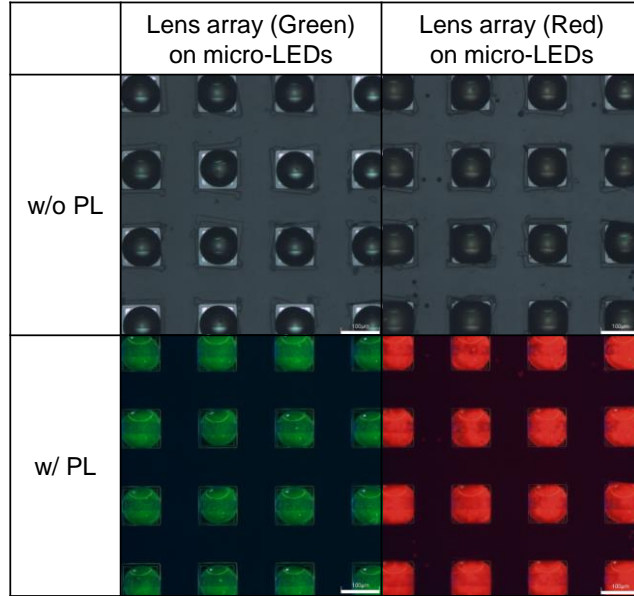
Figure 3.6. Photoluminescence images of the EHD printed green/red color-convertible microlens array with QD/polymer composite on the micro-LEDs (scale bar: 100 μm).
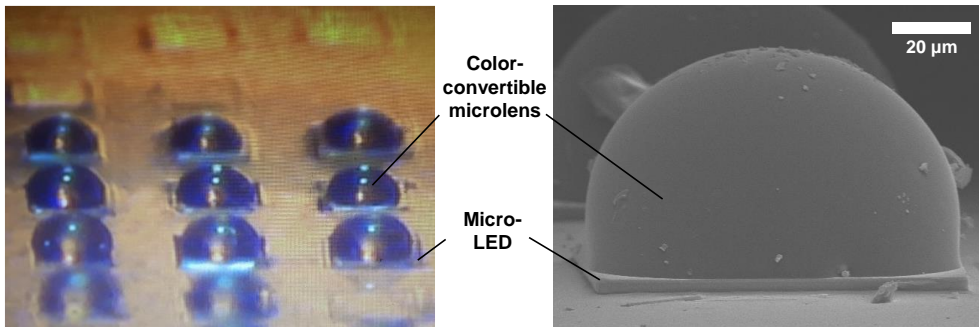
Figure 3.7. Camera and SEM images of the EHD printed color-convertible microlens array with QD/polymer composite on the micro-LEDs.
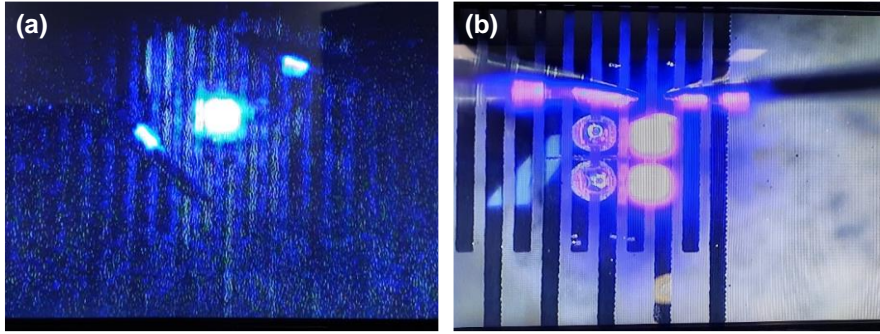
Figure 3.8. Camera images of down-converted light emission from the blue micro-LED with the (a) green and (b) red color-convertible microlens with QD/polymer composite.

LED. This is a common phenomenon in which liquids, as well as QD/NOA 61 composites, appear near the sharp edges on micropatterns [108], and there is a report of fabricated square shape lens arrays utilizing the pinning effect [109]. The fabrication of the color-convertible microlens array includes the same principle.

Figure 3.8 (a) and (b) show the down-conversion of blue light emitted from the micro-LED by connecting the micro-LED with the green and red color-convertible microlens to the electrode and driving it. The color shift is partially complete, so it looks like cyan when using green QD and magenta when using red QD. It is also confirmed from the measurement results in spectra and color coordinates. Figure 3.9 (a) shows the normalized PL spectra of light emitted from the blue LED, which is down-converted by green and red QD/NOA 61 composite as shown in Fig. 3.9 (b) and (c). Figure 3.9 (d) represents the 1931 CIE color coordinates of emitted light. It can be seen that the color conversion from blue to green or red is not completely achieved. This is due to the low blue light absorption characteristics of InP-based QD [110] and the leakage of blue light from the vertex of the micro-LED where the
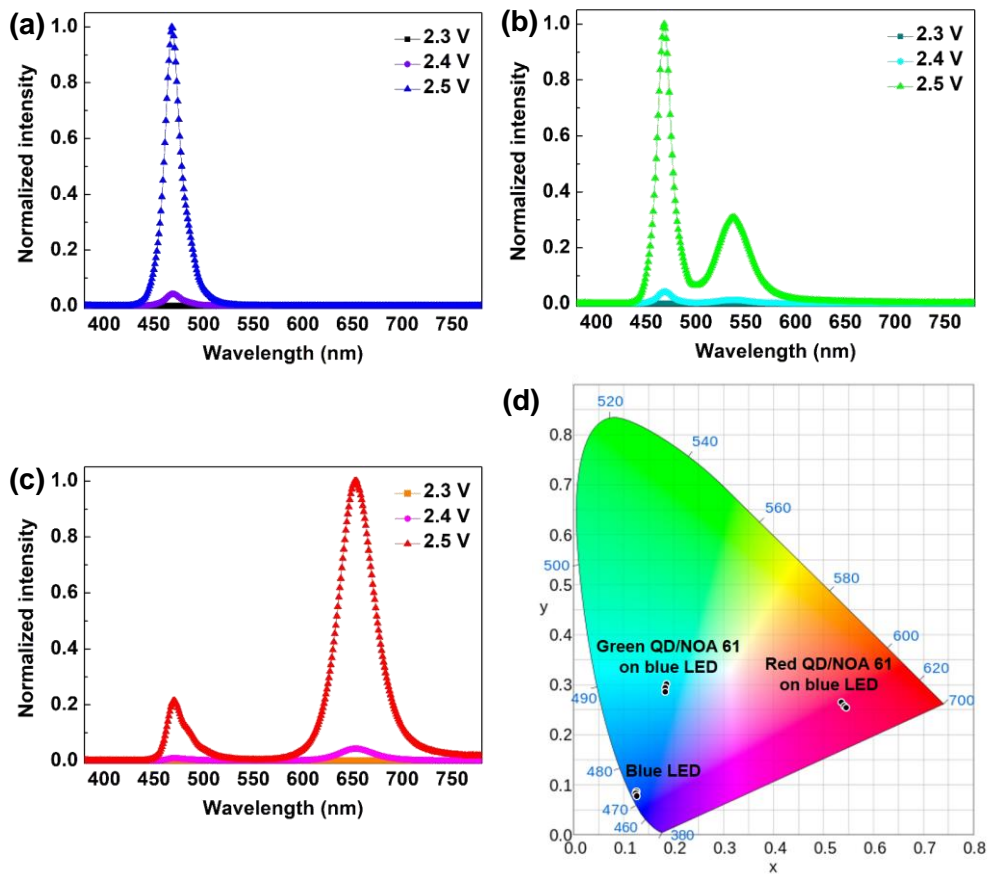
Figure 3.9. Normalized spectra of emitted light from the (a) blue LED, (b) green and (c) red QD/polymer composite on the blue LED according to driving voltage. (d) 1931 CIE color coordinates.

	Blue LED	Green QD solution	Red QD solution	Green QD/ NOA 61 on blue LED	Red QD/ NOA 61 on blue LED
Peak wavelength (nm)	468	525	626	537	653
FWHM (nm)	18	39	45	40	42

Table 3.2. Summarized optical properties of the peak wavelength and FWHM.

color-convertible microlens cannot cover. The color conversion ratio is defined as the number of photons converted to green or red to the number of blue photons emitted from the LED, and can be calculated as the following equation [111]:

$$(Color\ conversion\ ratio) = \frac{\sum \lambda I_{Conversion}}{\sum \lambda I_{Emission}} \qquad (\mathbf{3.3})$$

where $I_{Emission}$ is the intensity of emitted blue light, $I_{Conversion}$ is the intensity of light converted to green or red, and λ is the wavelength of light. According to Eq. (3.3), the color conversion ratios are calculated as 1.29 % for green and 3.43 % for red at 2.5 V driving voltage of the blue LED, which are insufficient values to be used as a pixel of micro-LED displays. To solve this problem, using an additional color filter or QD with high blue light absorbance can be solutions because the full-width at half maximum (FWHM) of the down-converted light is almost similar to that of the QD solution, thereby maintaining the color purity, as summarized in Table 3.2. It is also possible to adopt a micro-contact stamping as an auxiliary to completely cover the micro-LED with the color-convertible microlens.

3.3. Conclusion

In chapter 3.1, the method for implementing full-color micro-LED array, the types and characteristics of color converting materials, the material properties and patterning method of QD, and the principle of EHD printing for fine patterning are briefly reviewed. As an approach to solving the problems from previous researches, EHD printing of QD/photocurable polymer composite for a color filter with lens shape is reported in chapter 3.2. InP/ZnSeS/ZnS QD is adopted as the color converter, and NOA 61 is selected as polymer matrix materials. It is observed that the QD is well-dispersed when QD and NOA 61 are mixed at an optimized concentration. When the QD/NOA 61 composite is printed on a glass substrate or micro-LED, it becomes a hemispherical lens shape by the surface tension of the NOA 61. After that, the fabrication of a QD-embedded color-convertible microlens is completed by UV-curing, The formation of the color-convertible microlens is captured by PL and SEM images. The blue micro-LED with the color-convertible microlens is transferred to the metal electrode and operated. It is confirmed that the blue light emitted from the micro-LED is partially converted to red or green light.

The EHD-printed color-convertible microlens can be applied to various types of next-generation displays such as OLEDs and nanorod light-emitting diodes (NEDs) [112] as well as micro LEDs because it is possible to pattern in sub-micron scale with EHD printing. Therefore, the proposed concept in this chapter is expected to accelerate the development of the ultra-high-resolution display.

Chapter 4

Hierarchical Macro/Micro-scale Printed Optical Components

4.1. Introduction

This chapter introduces a tunable BIC eye structure with a combination of dispensing and dry-phase rubbing processes in a hierarchical macro/micro-scale. It is a representative optical component of a hierarchical structure that includes both macrolens and microlens, and this is the reason discussed in this chapter. The BIC eye mimics the unique optical structure in the insect's eye, and mainly consists of a curved microlens array, polymer cone, waveguide, and photodetector [113]. Researchers have been interested in its superior optical characteristics including wide field-of-view (FOV), low aberration, the nearly infinite depth of field (DoF), and high sensitivity to light for application to various optical systems such as biomedical endoscopies, surveillance cameras, and machine visions [114,115].

Due to the unique structure of the BIC eye, many studies focusing on the fabrication process have been conducted. Because microlens array should be included, conventional semiconductor fabrication processes such as thermal reflow

[116], wet etching [117], and laser writing [118] are used, as explained in chapter 2.1. After that, it is general to obtain a curved microlens array by replicating the planar microlens array with membrane form and then attaching it to a curved surface for thermosetting or applying pressure with the injection of fluid. However, since this approach involves a time-consuming and high-cost process associated with photolithography and etching, and it has disadvantages that the overall optical system becomes bulky and difficult to handle because maintenance for thermosetting or fluid injection should be required.

For fabricating microlens array without semiconductor fabrication processes, a method of using the self-assembly of microparticles in a liquid phase [119,120], which is called the Langmuir-Blodgett (LB) technique [121], has been considered. In this method, microparticles should be floated in the liquid media during the process. The microparticles are assembled on the surface of the macro-scale lens array, thereby forming hierarchical structures. This structure is used as a template and replicated with other materials to complete the BIC eye structures. However, this method is also required a liquid tank and not suitable for large-area fabrication. In addition, precise controlling of chemical properties such as pH and wettability of liquid is needed for obtaining a well-arranged monolayer of microparticles. Recently, dry-phase rubbing processes have been reported to assemble microparticles onto various types of surfaces including pre-patterned structure [122], flat [123], and curved surfaces [124] without liquid media. Microparticles are not mixed with any liquid and assembled by just applying small shear force with manually rubbing in a short time. Due to this advantage, the effective arrangement of microparticles and facile fabrication of microstructures is available with the dry-phase rubbing process.

The balance of adhesion force among microparticles, substrate, and rubbing materials is needed to obtain a well-arranged monolayer. Therefore, it is possible to form a microparticle monolayer selectively on the desired pattern, which is difficult to be achieved with the liquid-based LB technique. In the case of using nanoparticles, various structural colors can be observed according to the diameter and arrangement.

Another issue is that most BIC eye structures are fabricated with rigid materials. Their optical properties including focal length and FOV are fixed. In the case of a conventional spherical lens, this problem is solved by using elastomer as lens material for tunability of optical properties [125,126]. Based on this idea, several kinds of researches have also been reported in which BIC eye structure is made of soft materials, and then the optical properties are changed simply by applying an external stimulus. For example, there is a method of tuning the curvature of the lens array with hydraulic pressure by injecting a liquid [127]. Besides, approaches to changing the BIC eye structures by contracting and expanding it with electric potential [128], temperature [129], or pH [130] are also reported. However, the proposed methods have disadvantages in that a bulky and complex system is additionally required to applying external stimulus. When a voltage is applied, it should reach tens to several hundred volts, and it is difficult to control the flow rate when injecting liquid due to evaporation [131]. The materials of BIC can also be irreversibly changed. For these reasons, it is known that the mechanical tuning method is the simplest and has enhanced tunability and scalability.

With motivations as mentioned above, tunable BIC eye structure with soft materials fabricated by a combination of dispensing and dry-phase rubbing process in hierarchical macro/micro-scale is suggested and its characteristics are discussed.

4.2. Tunable Bio-inspired Compound Eye with Printing and Dry-phase Rubbing Process

4.2.1. Main Concept

Figure 4.1 shows a concept of the stretchable BIC eye structure. It is fabricated with elastomeric materials for securing intrinsic stretchability, and the shape of the macrolens is changed when mechanical strain is applied, thereby affecting the FOV. In general, FOV can be calculated by the following equation depending on the shape of the macrolens [118]

$$(FOV) = 2\,arcsin\left(\frac{2Rh}{R^2 + h^2}\right) \qquad (\mathbf{4.1})$$

where R and h are the radii and the height of the macrolens. According to Eq. (4.1), the R increases, and the h decreased when mechanical strain is applied to the stretchable BIC eye structure, thereby decreasing the FOV. By repeating stretching and releasing, the FOV can be easily tuned.
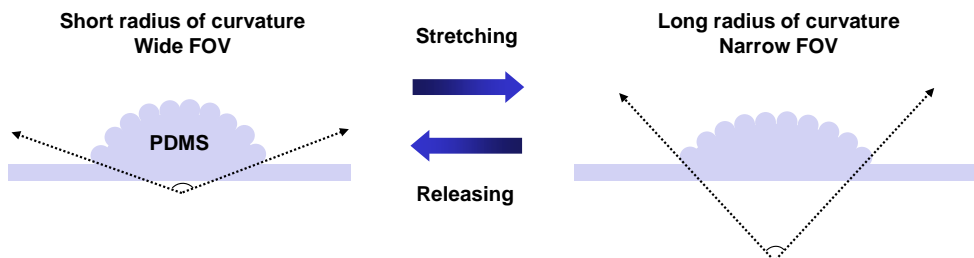
Figure 4.1. Schematic diagram of stretchable BIC eye structure with mechanical strain for tunable optical characteristics.

Microlens array on the surface of the macrolens is functionally related to light sensitivity, focusing of element images, and resolution of BIC eye structure. Especially, it also acts as a rigid island which is widely used in stretchable electronics [132] to protect devices by reducing external mechanical strain applied to the entire structure. Therefore, the shape of the microlens is hardly changed even if the shape of the macrolens is deformed. It means that the optical characteristics including the resolution and light sensitivity resulting from the shape of the microlens are almost maintained while adjusting the FOV by changing the shape of the macrolens.

The initial radius of the curvature of the macrolens is determined by the process temperature. The macrolens is fabricated by dispensing and curing PDMS. Because PDMS is a material cured by heat, so the higher temperature of the substrate, the less spreading and faster hardening [133], resulting in a larger contact angle and FOV. The radius of the microlens can be adjusted using microparticles of various radii. For BIC eye structure, the microlens generates element images for the object, so the size of microlens is closely related to the resolution of the image [117]. Therefore, it is possible to control the image resolution of BIC eye structures by changing the size of the microparticles. The density and signal sampling rate of microlens array is highest when arranged in a hexagonal close-packing (HCP) [51]. Since the microparticles are approximately arranged in the form of HCP by the dry-phase rubbing process, there is an advantage of the dry-phase rubbing process in terms of density of microlens array.

The proposed BIC eye structure has advantages such as facile fabrication method, controllability of resolution according to the microparticle size, and consisting of an elastomeric material, thereby realizing tunable optical properties.

4.2.2. Experimental Section

Figure 4.2 shows the fabrication process of the stretchable BIC eye structure. At first, PDMS liquid is obtained by mixing the PDMS base and curing agent (Sylgard 184, Dow Corning) at a weight ratio of 20:1 by centrifugal paste mixer (ARE-310, Thinky). The pre-cleaned glass substrate is placed on a hot plate at 120 ℃, followed by dispensing the PDMS liquid droplet and heat-curing for 30 min to form the shape of the macrolens. After that, the dried polystyrene (PS) microparticles (Analytical standard, 30 μm diameters, Sigma Aldrich) are rubbed manually and assembled on the surface of the macrolens selectively with the monolayer. FOTS (97 % assay, Sigma Aldrich) is exposed in the vapor by evaporation to the PDMS macrolens structure with a monolayer of PS microparticles for 30 min in a vacuum desiccator. The PDMS liquid is poured on the FOTS-treated template and heat-cured at 120 ℃ for 30 min. The first PDMS replica is completed by peeling off it from the template, followed by treating it with FOTS vapor again. To remove residual PS microparticle, the PDMS replica is cleaned with acetone by ultrasonication cleaner (Powersonic 620, Hwashin Technology) for 30 min and then dried at 50 ℃. The cleaned PDMS replica is treated with UV cleaner (AH-1700, Ahtech LTS) at 184 nm/254 nm wavelength and 30 mW/cm^2 intensity for 20 min, followed by FOTS surface treatment for 30 min. The PDMS liquid is poured on the surface-treated PDMS replica and thermally cured at 120 ℃ for 30 min again. Finally, the fabrication of the second PDMS replica is completed by peeling off it from the first PDMS replica, thereby obtaining BIC eye structure with PDMS.

The printed letter 'A' is placed under the BIC eye structure, and the images of
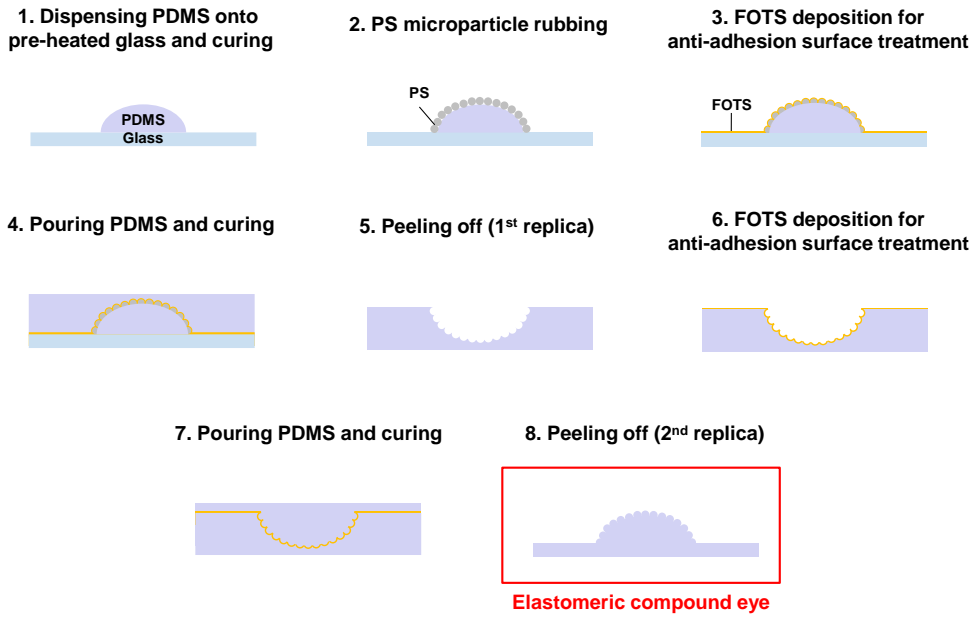
Figure 4.2. Fabrication process of a stretchable BIC eye structure.

the letter generated by microlens are captured by an optical microscope (DSX510, Olympus) at bright field mode. The BIC eye structure in oblique views is captured with a field emission scanning electron microscope (S-4800, Hitachi). The focal length of the microlens is calculated by using the lens maker equation or the difference of focused height between the image of the letter and the edge of the microlens [120,126]. For applying mechanical strain to the BIC eye structure, it is attached to the home-made stretchability test jig. The viewing angle is measured by placing the BIC eye structure on a stage that can be tilted from -30° to +30°. The strain analysis of the BIC eye structure is performed by finite element analysis (FEA) simulation software (COMSOL Multiphysics).

4.2.3. Results and Discussion

In Fig. 4.3, the overall sample image is captured by the camera, and the cross-sectional and top views of the edge and apex region of the BIC eye structure are shown with OM images. The values of diameter, height, and contact angle of the macrolens are 3270 μm, 380 μm, and 26°, respectively. The theoretical FOV is calculated as 52° according to Eq. (4.1), which is twice the value of the contact angle. Because the PS microparticles are arranged in a monolayer, a microlens array is formed well. The diameter of each microlens is about 30 μm, which is the same as that of the PS microparticles, indicating that replication is conducted successfully. In addition, since the PS microparticles are selectively placed on the PDMS macrolens surface, it is confirmed that the microlens array is also formed only on the PDMS macrolens surface. One of the important factors when rubbing microparticles is the adhesion strength between the microparticles and the substrate. If the adhesive strength is low, the microparticles tend to slide across the substrates. In contrast, the microparticles stick and tend to lose orders due to restricted translation if the adhesive strength is high. Therefore, the microparticles can roll and form a monolayer in the HCP arrangement under the appropriate adhesive strength. The images of the BIC eye structure from various views in detail are also captured by SEM, as shown in Fig. 4.4. The curved microlens array is uniformly formed on the surface of the macrolens. Through the microscopes observations, it is verified that the pattern of PDMS macrolens covered by PS microparticles monolayer is transferred into the PDMS replica without shape deformation. As a result, the BIC eye structure can be fabricated by the dispensing and dry-phase rubbing process.
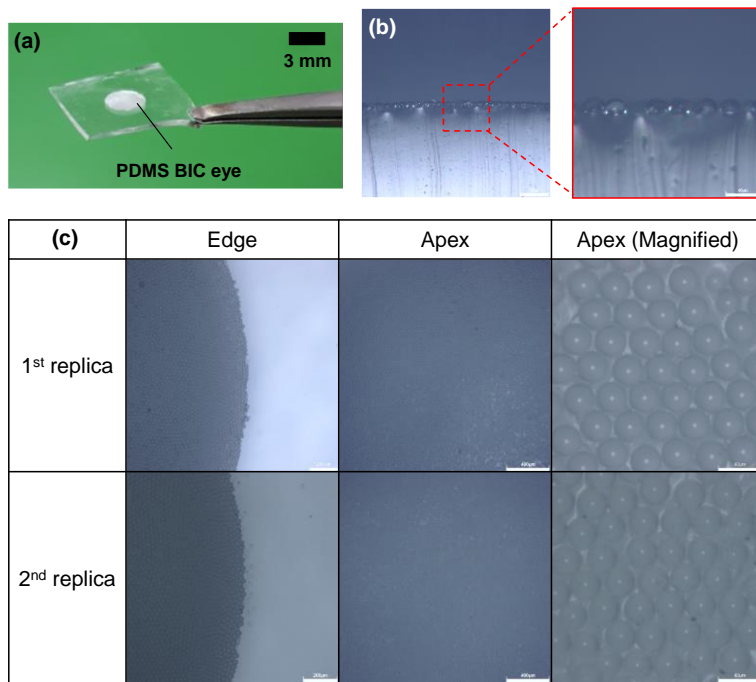
Figure 4.3. (a) Camera image of the PDMS BIC eye structure. OM images of the PDMS BIC eye structure from the (b) cross-sectional (scale bar: 40 µm) and (c) top view (scale bar: 200 µm for edge, 400 µm for apex, 40 µm for magnified apex).
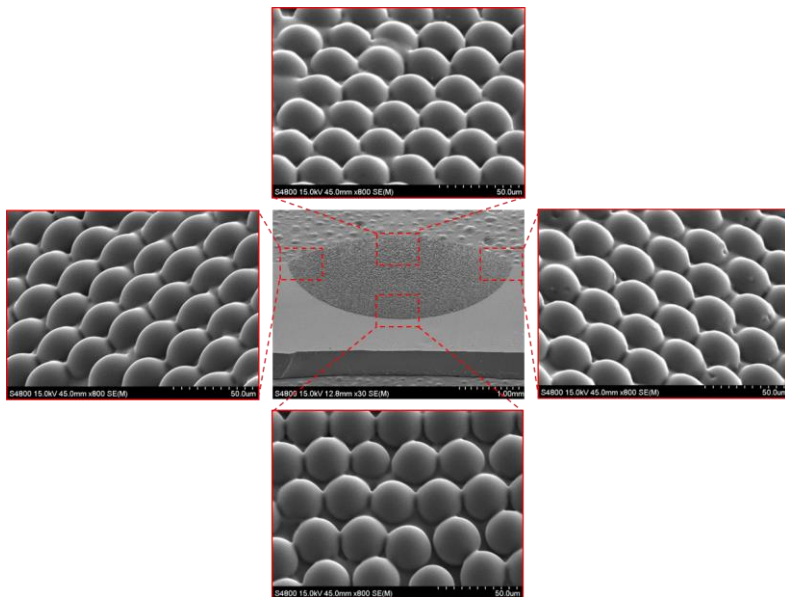
Figure 4.4. SEM images of the PDMS BIC eye structure from different views.
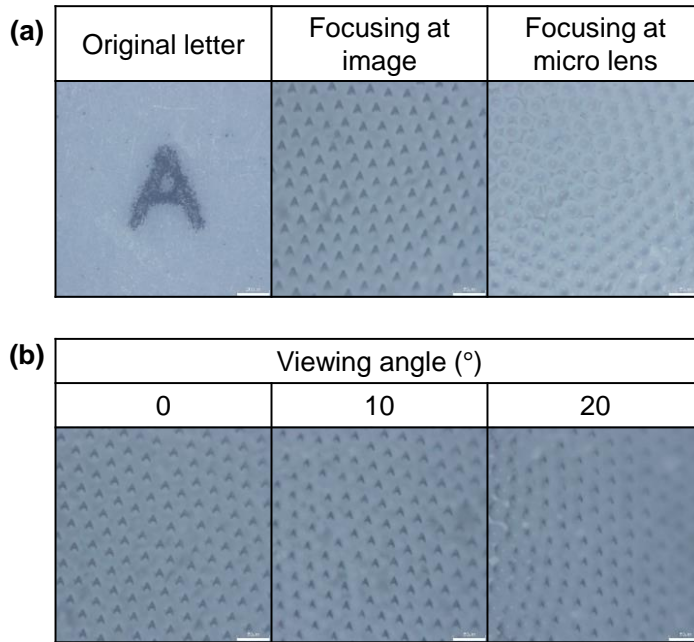
Figure 4.5. (a) Focused images generated by the microlens (scale bar: 200 μm for original letter, 50 μm for focusing at the image and microlens) and (b) observed with viewing angle range of ±20° (scale bar: 50 μm).

To check the imaging performances of the BIC eye structure, it is placed on the printed letter 'A' and observed with the OM where element images appear on each microlens, and the focused images are captured as shown in Fig. 4.5 (a). The focal length of the microlens is calculated by the difference in the position of the objective lens when focusing on the edge of the microlens and when the shape images appear. The calculated value is 37.5 μm, and it is compared with the value derived from the following lens maker equation.

$$f = \frac{R}{n-1} \tag{4.2}$$

where f, R, and n are the focal length, the radius, and the refractive index of the microlens. R is 15 μm, which is the radius of the PS microparticle, and n is 1.43, which is the refractive index of PDMS. By substituting these values into Eq. (4.2), the f is calculated as 40 μm. It can be confirmed that the focal lengths calculated by the objective lens position and the lens maker equation are similar to an error of 6.6 %. The causes of the error include a slight difference in the position of the objective lens and the assumption of paraxial rays in Eq. (4.2).

For the FOV measurement of the BIC eye structure, it is placed on a tilting stage and the focused images are observed by changing the tilting angle, as shown in Fig. 4.5 (b). When the stage is tilted by 10°, it is confirmed that the image is formed by each microlense in front of observation. As the inclination of the stage is about 20°, a region where the image formed by the microlens looks blurry appears, which means that the boundary of the FOV range has been reached. Therefore, the FOV is estimated at approximately 40°, which differs from the theoretical value of 52°. The reason is that the image by the microlens not immediately invisible as soon as exceeding the FOV range. It is not possible to determine an accurate FOV range with measurement because the image is gradually invisible and distorted severely in the vicinity of the boundary of the FOV range.

For investigating the role of the microlens as a rigid island on the curved surface of the macrolens, the 3D modeling of the BIC eye structure is established by FEA simulation based on measured geometric parameters, as shown in Fig. 4.6 (a). In particular, the diameter of the microlens is selected as 300 μm instead of 30 μm, because modeling with 30 μm microlens involves a huge computational load due to the large difference in scale with the macrolens, resulting in simulation failure.
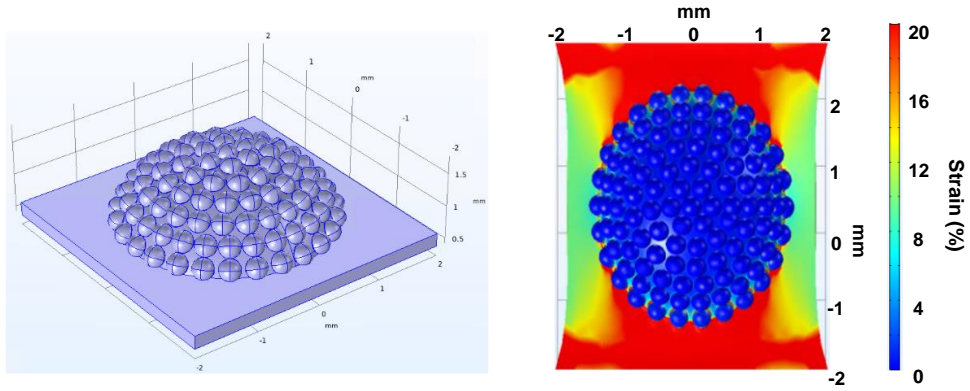
Figure 4.6. (a) 3D modeling for FEA simulation. (b) Simulation result of the strain distribution inside the PDMS BIC eye structure under 20 % uniaxial mechanical strain.

Since the macrolens already acts as a rigid island and the 300 μm microlens is modeled with the same aspect ratio as the 30 μm microlens, and the strain in the rigid island decreases as the size of the rigid island decreases [134], the strain-relief effect is indirectly proven even with a 30 μm microlens if the strain is reduced with a 300 μm microlens. Fig. 4.6 (b) shows the strain distribution within the entire BIC eyes structure when 20 % uniaxial mechanical strain is applied, and it is shown that there is almost no deformation in the microlens array.

Figure 4.7 shows OM images of the microlens and image size changes observed at the apex of the BIC eye structure while applying mechanical strain after attaching to the uniaxial stretching equipment. When the mechanical strain is applied to the BIC eye structure uniaxially, the circular microlens is deformed into an elliptical shape [135], the local strain along the direction of external mechanical strain is calculated by comparing the long axis length of the elliptical microlens and the diameter of the circular microlens.

Strain (%)	0	20	40	60
Stretched BIC eye				
Focusing at image				
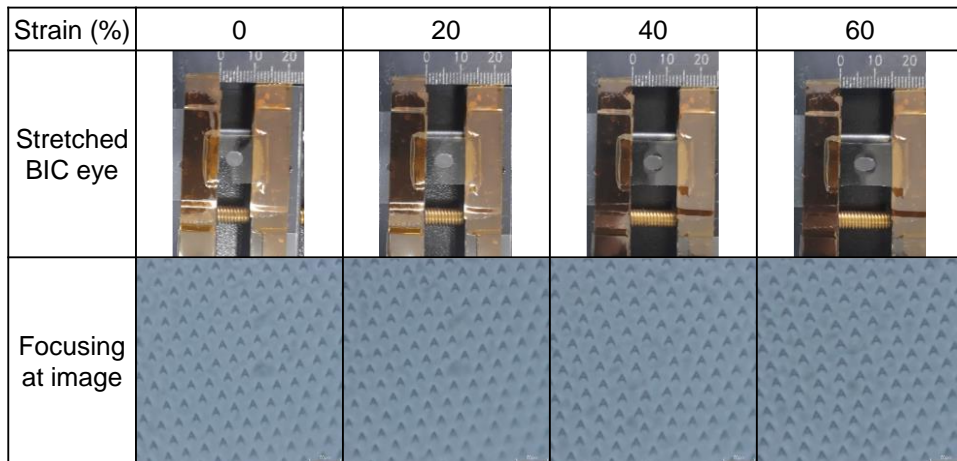
Figure 4.7. Focused images generated by the microlens according to uniaxial external strain (scale bar: 50 µm).

When applying 20 % mechanical strain, the local strain applied in the same direction is about 2.57 %, which is consistent with the result of the strain distribution simulation. For the 40 % and 60 % mechanical strain, the local strain is measured at 10.26 % and 15.73 %, respectively. Although there are still strain-relief effects, the local strain itself increases rapidly compared to the case of 20 % mechanical strain. Therefore, it can be concluded that it is appropriate to tune the BIC eye structure fabricated in this experiment within a mechanical strain of 20 %, and this range can be changed depending on the size and thickness of the BIC eye structure. When the circular microlens is deformed into an elliptical microlens by uniaxial stretching, the focal spot is also changed to elliptical shape due to the different focal length of the major and minor axis direction [135]. Since the focal spot affects the design of the imaging device, the circular focal spot can be maintained by applying biaxial stretching for uniform focusing characteristics.

4.3. Conclusion

The characteristics and previous researches of the BIC eye structure are briefly introduced in chapter 4.1. Based on the issues related to the fabrication process and tunability of optical properties, the concept of tunable BIC eye structure with a combination of a dispensing and dry-phase rubbing processes in hierarchical macro/micro-scale is suggested in chapter 4.2. A hemispherical PDMS macrolens is formed by the dispensing method, followed by the dry-phase rubbing process for assembling PS microparticles in monolayer onto the curved surface of the PDMS macrolens. This hierarchical structure is used as a template and is replicated in PDMS for the intrinsic stretchability of the BIC eye structure. The fabrication and measurement results of the BIC eye structure are also discussed. Microlens array is formed on the surface of the macrolens and acts as a rigid island, thereby maintaining microlens shape and its optical characteristics when mechanical strain is applied to overall BIC eye structure even though the shape of the macrolens is changed.

It is presented the possibility that complex shapes like hierarchical structure can be produced only by additive manufacturing without a conventional semiconductor fabrication process and applied to optical systems through the work investigated in this chapter. It is expected that the printed tunable optical components have the potential to be utilized in various types of imaging systems in a simple and cost-effective method.

Chapter 5

Conclusion

5.1. Summary

Throughout the whole chapter in this dissertation, the 3D printing-based customized optical components are proposed for display and imaging system applications. An additive manufacturing process is an approach to building a structure by adding materials and has the advantage of facile fabrication of complex structures. It includes ink jetting-based methods such as FDM and DIW and light curing-based methods such as SLA and SLS, and appropriate methods can be selected according to the material, resolution, and desired applications. Due to simple maintenance requirements and short process time, it is widely utilized to manufacture products in various fields such as mechanical components, biomedical organ, and architectural modeling. Other promising applications for additive manufacturing are electronic devices and optical components, which are typically fabricated by a conventional semiconductor process. However, these are still limited to production in research and development steps. In particular, although there have been many reports about fabrication and evaluation of additive manufactured optical components in recent

years, there are few cases which implementing their practical applications because there are additional considerations only when manufacturing optical components such as adopting highly transparent or reflective materials and surface planarization under a roughness of tens of micrometers. It is required for investigating the potential usefulness for printed optical components, to achieve better performance, productivity, and usability in three aspects including a wide range of length scale, complex structures, and tunable functionality. Based on these motivations, several types of printed optical components and their display and imaging system applications are presented in this dissertation to show the scalability of printing with macro-scale, micro-scale, and hierarchical macro/micro-scale.

As macro-scale printed optical components, lens and mirror are adopted for seamless modular display applications. The cylindrical lens pair is fabricated by the dispensing method and utilized for the demonstration of a seamless modular flat panel display. Also, the concave mirror is fabricated from FDM-type 3D printed mold, followed by being used for implementing the seamless modular curved-edge display. By attaching a printed lens or mirror onto the seam of the modular display, the applicability of seamless modular display technology with the various form factor of the panel is suggested in the facile and cost-effective approach.

In micro-scale printing, the color-convertible microlens is chosen for full-color micro-LED array applications. By EHD printing of QD/photocurable polymer composite, QD-embedded hemispherical microlens shape is formed on a glass substrate and blue micro-LED array by adjusting printing conditions. InP/ZnSeS/ZnS QD is used as the color converting materials, and NOA 61 is selected as a photocurable polymer. When the blue micro-LED with the color-convertible

microlens is operated, the blue light emitted from the micro-LED is partially converted to red or green light, thereby showing the application to the ultra-high-resolution micro-LED display.

Finally, the BIC eye structure is introduced as a hierarchical macro/micro-scale printed optical component. It is fabricated by a combination of PDMS dispensing and PS microparticles dry-phase rubbing process. The hierarchical structure with PS microparticles on PDMS macrolens is replicated in PDMS, resulting in forming the BIC eye structure. The imaging performance and strain distribution under the uniaxial deformation of the BIC eye structure are also discussed. It is expected that printed optical components with soft materials can be formed with complex shapes and applied to optical systems in a simple method.

5.2. Limitations and Suggestions for Future Researches

Lastly, the limitations and suggestions for future researches in the field of printed optical components and their promising applications are discussed in this chapter, which is the final session of the dissertation.

(1) Printed lens and mirror: When implementing the seamless modular display with a lens or mirror, image distortion inevitably occurs due to the magnification of the original image. To alleviate the image distortion, pre-compensation images via light field optimization [136], which is a method for enhancing image quality in a 3D display, can be utilized. This computational optimization minimizes the difference between the target and the actual image. Once the optimization is completed in the particular display system, it is universally applicable to other identical display systems. As the pixel gets smaller, it is difficult for humans to recognize it even if it is magnified, as shown in Fig. 5.1. Therefore, the tiling of high-resolution screens including micro-LED display [137] can be a promising method for demonstrating seamless modular display with minimized image distortion.
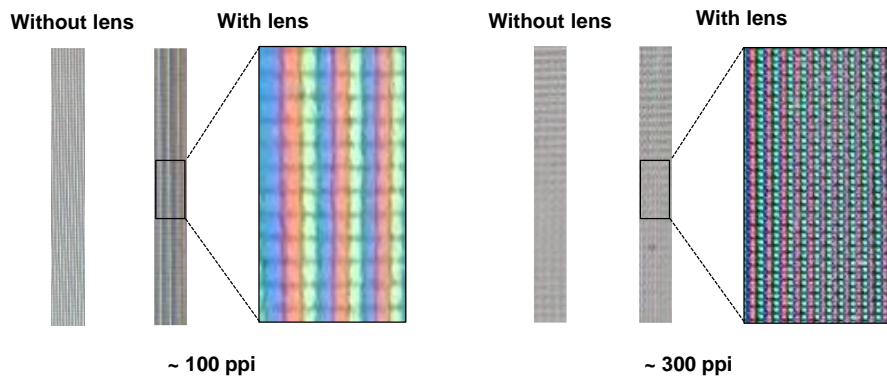
Figure 5.1. 100 and 300 ppi R/G/B pixels magnified by the printed cylindrical lens.
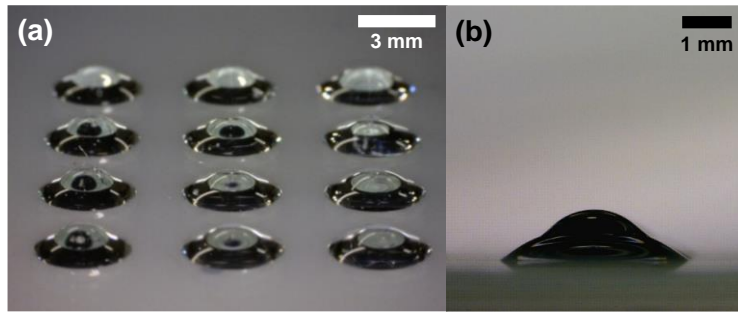
Figure 5.2. Camera images of the printed lens-on-lens structure from the (a) oblique (b) cross-sectional view.

In addition, since chromatic aberration also occurs, using a material with a small Abbe number, which represents the wavelength dependence of reflective index, can be an alternative as a lens material such as polycarbonate (PC) and polysulfone (PSU) [138].

Another problem is that the lens and mirror are the height of a few millimeters, so these are bulky on the display. Also, the visibility of the boundary line between the printed optical components and the display should be reduced. To solve these issues, it is expected that the use of flat optics components such as diffractive lenses [139] and metalenses [140] can be alternatives. To fabricate the planar lens, it is necessary to increase the resolution of 3D printing maintenance.

For further applications, there is a case of manufacturing a foveated lens using 3D printing for the AR display application [141]. It is possible to manufacture a lens with an unusual shape like a lens-on-lens structure by dispensing method, as shown in Fig. 5.2. It can be applied to image depth representation due to dual-focusing characteristics [142]. In the case of mirrors, a reflective dynamic display that pneumatically adjusts the surface roughness of the mirror layer is reported [143].

From these examples, optical components printed with macro-scale show various applications beyond the seamless modular displays.

(2) Printed color-convertible microlens: Although InP-based QD has emerged as a promising eco-friendly material, it has still low stability and quantum yield for color conversion or emitting layer in LED. To improve the optical characteristics of InP-based QD, there have been attempts to increase efficiency by optimizing shell thickness and adding an element like Ga to form an alloyed-QD.

Furthermore, there is an approach to combine the advantages of QD and phosphor by preparing a QD/phosphor composite [144]. For EHD printing of QD/phosphor composite in the form of the color-convertible microlens, nanometer-sized phosphor [145] should be used. It is also possible to add blue light-absorbing materials [146] in the QD-based composite to prevent blue light from leakage.

Another challenge is the nano-scale patterning of QD/polymer composite for full-color nano-LED display application, as mentioned in chapter 3.3. Recently, the nano pixels with QD/polymer composite fabricated by 3D printing is reported [147]. This approach is expected to be applied to the fabrication of color conversion or emitting layer of the nano-LED in the future. For micro/nano-scale printing, the high dispersibility of QD in the polymer matrix is required to be stable jetting without clogging, and synthesis of the appropriate ligand for well-dispersion is a general approach with surface engineering. An approach of uniformly anchoring the QD with liquid crystal (LC) matrix [148] is also a remarkable method.

If a viscous liquid is jetted continuously during EHD printing, the shape of the cylindrical microlens is well-formed. It can be applied to micro-optical systems such as optical waveguide [149] and one-dimensional (1D) color filter in the microscope
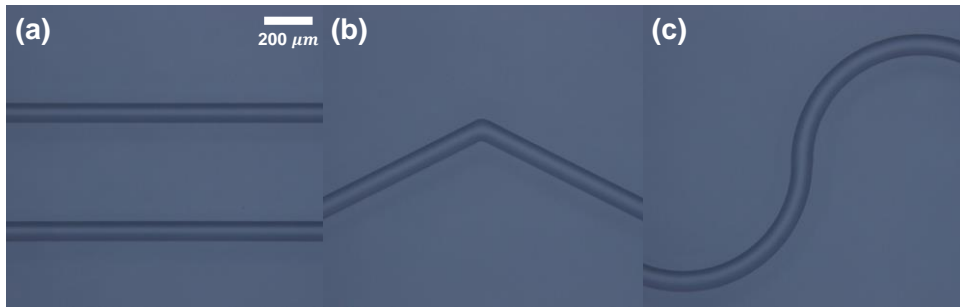
Figure 5.3. OM images of the EHD printed optical waveguides: (a) straight line, (b) triangular, and (c) circular shape.

system [150]. Figure 5.3 (a)-(c) show EHD printed optical waveguide as examples. Furthermore, it is expected that the EHD printing makes it easy to fabricate a multifocal microlens array [151] for extended DoF on a single substrate. Through the examples as mentioned, optical components printed with micro-scale have various applications beyond the micro-LED displays.

(3) Printed bio-inspired compound eye: A representative application of the BIC eye structure is the lens module of the image sensor. However, most commercialized image sensors are flat, resulting in the appearance of a sharp image only in a central region on the image sensor due to the curved focal plane generated by a curved microlens array on the macrolens surface in the BIC eye structure. To solve this problem, there are methods of fabricating microlens arrays of different focal length [152] according to the region of the BIC eye structure or embedding a microprism structure [153] to align the focal plane with a flat image sensor. The integration of the curved image sensor to match it to the curved focal plane is an alternative [114], but it is still difficult to fabricate electronic devices on a curved surface. Therefore, the development of stretchable electronics on the curved substrate should be

achieved together for the imaging system applications of the BIC eye structure.

Another problem to be solved with the BIC eye structure is its low transparency and adsorption of moisture. One of the methods to solve this problem is an approach that implements superhydrophobic and antireflective surfaces by fabricating the tertiary structure of macro/micro/nano-scale lenses [154]. If the dry-phase rubbing of nanoparticles is added to the process introduced in chapter 4.2.2, a more functional BIC eye structure can be fabricated by additive manufacturing. For more applications, the BIC eye structure can be also integrated with LEDs for light extraction enhancement [155] in highly efficient display and lighting devices.

In this dissertation, the enabling technologies for 3D printed optical components with wide scalability are introduced. Optical components will be manufactured more easily as 3D printing maintenances become cheaper and more precise, and the field of 'consumer optics [138]' or 'DIY optics [156]' will be more active. Furthermore, it will also be simple to create components for deformable [157] and multi-scale [158] optical systems with unique characteristics. It is expected that this dissertation can contribute to establishing a guideline and paving the way for 3D printed optical components in next-generation display and imaging system applications.

References

[1]   A. Amborsi, M. Pumera. 3D-printing technologies for electrochemical applications. *Chem. Soc. Rev*. **45**, 2740-2755 (2016).

[2]   T. Sathish, M. D. Vijayakumar, A. K. Ayyangar. Design and fabrication of industrial components using 3D printing. *Mater. Today Proc*. **5**, 14489-14498 (2018).

[3]   G. T. Carranza, U. Robles, C. L. Valle, J. J. Gutierrez, R. C. Rumpf. Design and hybrid additive manufacturing of 3-D/volumetric electrical circuits. *IEEE Trans. Compon. Packag. Manuf. Technol*. **9**, 1176-1183 (2019).

[4]   N. Hack, W. V. Lauer. Mesh-mould: Robotically fabricated spatial meshes as reinforced concrete formwork. *Archit. Des*. **84**, 44-53 (2014).

[5]   J. W. Jung, J. –S. Lee, D. –W. Cho. Computer-aided multiple-head 3D printing system for printing of heterogeneous organ/tissue constructs. *Sci. Rep*. **6**, 21685 (2016).

[6]   O. A. Mohamed. *Analytical modeling and experimental investigation of product quality and mechanical properties in FDM additive manufacturing*. Ph. D. Thesis, Swinburne University of Technology (2017).

[7]   R. L. Truby, J. A. Lewis. Printing soft matter in three dimensions. *Nature* **540**, 371-378 (2016).

[8]   R. Melnikova, A. Ehrmann, K. Finsterbusch. 3D printing of textile-based structures by fused deposition modeling (FDM) with different polymer materials. *IOP Conf. Ser.: Mater. Sci. Eng*. **62**, 012018 (2014).

[9]   B. Derby. Inkjet printing of functional and structural materials: Fluid property

requirements, feature stability, and resolution. *Annu. Rev. Mater. Res.* **40**, 395-414 (2010).

[10] J. –U. Park, M. Hardy, S. J. Kang, K. Barton, K. Adair, D. K. Mukhopadhyay, C. Y. Lee, M. S. Strano, A. G. Alleyne, J. G. Georgiadis, P. M. Ferreira, J. A. Rogers. High-resolution electrohydrodynamic jet printing. *Nat. Mater.* **6**, 782-789 (2007).

[11] X. Zhang, X. N. Jiang, C. Sun. Micro-stereolithography of polymeric and ceramic microstructures. *Sens. Actuator A* **77**, 149-156 (1999).

[12] J. –P. Kruth, P. Mercelis, J. V. Vaerenbergh, L. Froyen, M. Rombouts. Binding mechanisms in selective laser sintering and selective laser melting. *Rapid Prototyp. J.* **11**, 26-36 (2005).

[13] B. H. Cumpston, S. P. Ananthavel, S. Barlow, D. L. Dyer, J. E. Ehrlich, L. L. Erskine, A. A. Heikal, S. M. Kuebler, I. –Y. S. Lee, D. McCord-Maughon. J. Qin, H. Röckel, M. Rumi, X. –L. Wu, S. R. Marder. J. W. Perry. Two-photon polymerization initiators for three-dimensional optical data storage and microfabrication. *Nature* **398**, 51-54 (1999).

[14] S. Chung, M. A. U. Karim, H. –J. Kwon, V. Subramanian. High-performance inkjet-printed four-terminal microelectromechanical relays and inverters. *Nano. Lett.* **15**, 3261-3266 (2015).

[15] J. Ha, J. Seo, S. Lee, E. Oh, T. Lee, S. Chung, Y. Hong. Efficient surface treatment to improve contact properties of inkjet-printed short-channel organic thin-film transistors. *J. Nanosci. Nanotechnol.* **17**, 5718-5721 (2017).

[16] G. D. Berglund, T. S. Tkaczyk. Fabrication of optical components using a consumer-grade lithographic printer. *Opt. Express* **27**, 30405-30420 (2019).

[17]   S. S. Hinman, K. S. McKeating, Q. Cheng. Plasmonic sensing with 3D printed optics. *Anal. Chem*. **89**, 12626-12630 (2017).

[18]   N. Vaidya, O. Solgaard. 3D printed optics with nanometer scale surface roughness. *Microsyst. Nanoeng.* **4**, 18 (2018).

[19]   *Inkjet functional and additive manufacturing for electronics report*, Yole Development (2018).

[20]   K. –C. Fan, J. –Y. Chen, C. –H. Wang, W. –C. Pan. Development of a drop-on-demand droplet generator for one-drop-fill technology. *Sens. Actuators A* **147**, 649-655 (2008).

[21]   N. Chopra, M. Su, C. Madigan. Inkjet printing applications in next generation OLED and QD TV. in *International Meeting on Information Display* (2019).

[22]   J. Souk, S. Morozumi, F. –C. Luo, I. Bita. *Flat panel display manufacturing* (John Wiley & Sons, 2018).

[23]   A. C. Arias, J. D. MacKenzei, I. McCulloch, J. Rivnay, A. Salleo. Materials and applications for large area electronics: Solution-based approaches. *Chem. Rev.* **110**, 3-24 (2010).

[24]   M. Aston. Design of large-area OLED displays utilizing seamless tiled components. *J. Soc. Inf. Disp.* **15**, 535-540 (2007).

[25]   K. M. Kim, I. Han, S. Noh, Y. I. Jang, K. Oh, B. Kim, I. –B. Kang. Bezel free design of organic light emitting diode display via a-InGaZnO gate driver circuit integration within active array. *J. Soc. Inf. Disp*. **27**, 514-522 (2019).

[26]   S. Lee, S. Lee, H. Yoon, C. –K. Lee, C. Yoo, J. Park, J. Byun, G. Kim, B. Lee, B. Lee, Y. Hong. Printed cylindrical lens pair for application to the seam concealment in tiled displays. *Opt. Express* **26**, 824-834 (2018).

[27] S. Lee, J. Moon, S. Yang, J. Rhim, B. Kim, Y. Lee, S. Han, S. Yoon, I. Kang. Development of zero-bezel display utilizing a waveguide image transformation element. *SID Symp. Dig. Tech. Papers* **48**, 612-614 (2017).

[28] X. C. Shan, T. Liu, M. Mohaime, B. Salam, Y. C. Liu. Large format cylindrical lens films formed by roll-to-roll ultraviolet embossing and applications as diffusion films. *J. Micromech. Microeng.* **25**, 035029 (2015).

[29] M. F. Schumann, S. Wiesendanger, J. C. Goldschmidt, B. Bläsi, K. Bittkau, U. W. Paetzold, A. Sprafke, R. B. Wehrspohn, C. Rockstuhl, M. Wegener. Cloaked contact grids on solar cells by coordinate transformations: Designs and prototypes. *Optica* **2**, 850-853 (2015).

[30] M. Ashraf, C. Gupta, F. Chollet, S. V. Springham, R. S. Rawat. Geometrical characterization techniques for microlens made by thermal reflow of photoresist cylinder. *Opt. Laser Eng.* **46**, 711-720 (2008).

[31] J. Albero, L. Nieradko, C. Gorecki, H. Ottevaere, V. Gomez, H. Thienpont, J. Pietarinen, B.Päivänranta, N. Passilly. Fabrication of spherical microlenses by a combination of isotropic wet etching of silicon and molding techniques. *Opt. Express* **17**, 6283-6292 (2009).

[32] D. Wu, S. –Z. Wu, L. –G. Niu, Q. –D. Chen, R. Wang, J. –F. Song, H. –H. Fang, H. –B. Sun. High numerical aperture microlens arrays of close packing. *Appl. Phys. Lett.* **97**, 031109 (2010).

[33] C. T. Pan, T. T. Wu, M. F. Chen, Y. C. Chang, C. J. Lee, J. C. Huang. Hot embossing of micro-lens array on bulk metallic glass. *Sens. Actuator A* **141**, 422-431 (2008).

[34] E. Fortunato, P. Barquinda, R. Martins. Oxide semiconductor thin-film

transistors: A review of recent advances. *Adv. Mater.* **24**. 2945-2986 (2012).

[35] J. Y. Kim, K. Pfeiffer, A. Voigt, G. Gruetzner, J. Brugger. Directly fabricated multi-scale microlens arrays on a hydrophobic flat surface by a simple ink-jet printing technique. *J. Mater. Chem.* **22**, 3053-3058 (2012).

[36] A. C. Roy, M. Yadav, E. P. Arul, A. Khanna, A. Ghatak. Generation of aspherical optical lenses via arrested spreading and pinching of a cross-linkable liquid. *Langmuir* **32**, 5356-5364 (2016).

[37] B. –J. De Gans, P. C. Duineveld, U. S. Schubert. Inkjet printing of polymer: State of the art and future development. *Adv. Mater.* **16**, 203-213 (2004).

[38] J. Xing, W. Rong, D. Sun, L. Wang, L. Sun. Extrusion printing for fabrication of spherical and cylindrical microlens arrays. *Appl. Opt.* **55**, 6947-6952 (2016).

[39] H. Kim, J. Kim, J. Kim, B. Lee, S. –D. Lee. Liquid crystal-based lenticular lens array with laterally shifting capability of the focusing effect for autostereoscopic displays. *Opt. Commun.* **357**, 52-57 (2015).

[40] K. Kimura, S. Hasegawa, Y. Hayasaki. Diffractive spatiotemporal lens with wavelength dispersion compensation. *Opt. Lett.* **35**, 139-141 (2010).

[41] V. C. Coffey. The age of OLED displays. *Opt. Photonics News* **28**, 34 (2017).

[42] K. D. Powell, J. M. Lutian. *Curved edge display with controlled luminance*. US Patent 10,185,064 B2 (Jan. 22, 2019).

[43] J. Hong, Y. Kim, S. –G. Park, J. –H. Hong, S. –W. Min, S. –D. Lee, B. Lee. 3D/2D convertible projection-type integral imaging using concave half mirror array. *Opt. Express* **18**, 20628-20637 (2010).

[44] X. Wu, Y. Wu, P. Wen. Concave omnidirectional imaging device for cylindrical object based on catadioptric panoramic imaging. *Opt. Eng.* **57**,

033109 (2018).

[45] Y. M. Sabry, D. Khalil, B. Saadany, T. Bourouina. Integrated wide-angle scanner based on translating a curved mirror of acylindrical shape. *Opt. Express* **21**, 13906-13916 (2013).

[46] M. Schaub, J. Schwiegerling, E. C. Fest, A. Symmons, R. H. Shepard. *Molded Optics: Design and Manufacture* (CRC Press, 2011).

[47] K. Mishra, C. Murade, B. Carreel, I. Roghair, J. M. Oh, G. Manukyan, D. van den Ende, F. Mugele. Optofluidic lens with tunable focal length and asphericity. *Sci. Rep*. **4**, 6378 (2014).

[48] H. A. Elagha. Generalized formulas for ray-tracing and longitudinal spherical aberration. *J. Opt. Soc. Am. A*. **34**, 335-343 (2017).

[49] J. Kim, Y. Jeong, H. Kim, C. –K. Lee, B. Lee, J. Hong, Y. Kim, Y. Hong, S. – D. Lee, B. Lee. F-number matching method in light field microscopy using an elastic micro lens array. *Opt. Lett.* **41**, 2751-2754 (2016).

[50] D. Xie. H. Zhang, X. Shu, J. Xiao. Fabrication of polymer micro-lens array with pneumatically diaphragm-driven drop-on-demand inkjet technology. *Opt. Express* **20**, 15186-15195 (2012).

[51] T. Hou, C. Zheng, S. Bai, Q. Ma, D. Bridges, A. Hu, W. W. Duley. Fabrication, characterization, and applications of microlenses. *Appl. Opt.* **54**, 7366-7376 (2015).

[52] E. P. Dupont, R. Luisier, M. A. M. Gijs. NOA 63 as a UV-curable material for fabrication of microfluidic channels with native hydrophilicity. *Microelectron. Eng.* **87**, 1253-1255 (2010).

[53] H. Shim, I. Kee, S. Kim, Y. Chun, H. Kwon, Y. Jin, S. Lee, D. Han, J. Kwack,

D. Kang, H. Seo, M. Song, M. Lee, S. Kim. A New seamless foldable OLED display composed of multi display panels. *SID Symp. Dig. Tech. Papers* **41**, 257-260 (2010).

[54] M.-H. Shin, J.-Y. Lee, H.-R. Moon, Y.-J. Kim. Proposal and design of hybrid light guide plate based on aspheric concave surface and micropatterns to improve illuminance and color uniformity for LED display. *Jpn. J. Appl. Phys.* **53**, 08MF01 (2014).

[55] Q. Feng, Q. Li, Y. Wang, C. Wu, G. Lv. The design and optimization of lens array for LED backlight in LCD imaging engine of helmet-mounted display. *J. Soc. Inf. Disp.* **25**, 312–319 (2017).

[56] M. E. Becker. Measurement of visual resolution of display screens. *SID Symp. Dig. Tech. Papers* **48**, 915-918 (2017).

[57] W. J. Smith. *Modern Optical Engineering* (McGrawHill, 2000).

[58] G. A. Alphonse, J. Lubin. Psychophysical requirement for tiled large screen displays. *Proc. SPIE* **1664**, 230-240 (1992).

[59] C. Blanc, C. Schlick. Accurate parametrization of conics by NURBS. *IEEE Comput. Graph. Appl.* **16**, 64-71 (1996).

[60] X. Chen, G. Chen, G. Wang, P. Zhu, C. Gao. Recent progress on 3D-printed polylactic acid and its applications in bone repair. *Adv. Eng. Mater.* **22**, 1901065 (2020).

[61] B. Kang, J. Sung, H. So. Realization of superhydrophobic surfaces based on three-dimensional printing technology. *Int. J. of Precis. Eng. and Manuf. - Green Tech.* **8**, 47-55 (2021).

[62] X. –Q. Liu, S. –N. Yang, Y. –L. Sun, L. Yu, B. –F. Bai, Q. –D. Chen, H. –B.

Sun. Ultra-smooth micro-optical components of various geometries. *Opt. Lett*. **44**, 2454-2457 (2019).

[63] X. Chen, W. Liu, B. Dong, J. Lee, H. O. T. Ware, H. F. Zhang, C. Sun. High-speed 3D printing of millimeter-size customized aspheric imaging lenses with sub 7 nm surface roughness. *Adv. Mater*. **30**, 1705683 (2018).

[64] H. E. Bennett, J. O. Porteus. Relation between surface roughness and specular reflectance at normal incidence. *J. Opt. Soc. Am*. **51**, 123-129 (1961).

[65] N. Bowden, S. Brittain, A. G. Evans, J. W. Hutchinson, G. M. Whitesides. Spontaneous formation of ordered structure in thin films of metals supported on an elastomeric polymer. *Nature* **393**, 146-149 (1998).

[66] K. Efimenko, W. E. Wallace, J. Genzer. Surface modification of Sylgard-184 poly(dimethyl siloxane) networks by ultraviolet and ultraviolet/ozone treatment. *J. Colloid Interface Sci.* **254,** 306-315 (2002).

[67] E. Barkman. Specular and diffuse reflectance measurements of aluminum surface. *Appearance of Metallic Surfaces*, ASTM STP **478**, 46-58 (1970).

[68] S. –A. Tsai, H. –C. Wei, G. –D. J. Su. Polydimethylsiloxane coating on an ionic polymer metallic composite for a tunable focusing mirror. *Appl. Opt*. **51**. 8315-8323 (2012).

[69] L. Spencer, M. Jakobsen, S. Shah, G. Cairns. Minimum required angular resolution of smartphone displays for the human visual system. *J. Soc. Inf. Disp.* **21**, 352-360 (2013).

[70] Y. Huang, E. –L. Hsiang, M. –Y. Deng, S. –T. Wu. Mini-LED, micro-LED and OLED displays: Present status and future perspectives. *Light Sci. Appl*. **9**, 105 (2020).

[71] G. Hass. Microdisplays for wearable augmented reality – OLED vs LED based systems. *SID Symp. Dig. Tech. Papers* **50**, 713-716 (2019).

[72] J. J. D. McKendry, D. Massoubre, S. Zhang, B. R. Rae, R. P. Green, E. Gu, R. K. Henderson, A. E. Kelly, M. D. Dawson. Visible-light communications using a CMOS-controlled micro-light-emitting-diode array. *J. Lightwave Technol.* **30**, 61-67 (2012).

[73] X. Bi, T. Xie, B. Fan, W. Khan, Y. Guo, W. Li. A flexible, micro-lens-coupled LED stimulator for optical neuromodulation. *IEEE Trans. Biomed. Circuits Syst.* **10**, 972-978 (2016).

[74] W. H. Kim, Y. J. Jang, J. –Y. Kim, M. Han, M. Kang. K. Yang, J. –H. Ryou, M. –K. Kwon. High-performance color-converted full-color micro-LED arrays. *Appl. Sci*. **10**, 2112 (2020).

[75] R. S. Cok, M. Meitl, R. Rotzoll, G. Melnik, A. Recioru, A. J. Trindade, B. Raymond, S. Bonafede, D. Gomez, T. Moore, C. Prevatte, E. Radauscher, S. Goodwin, P. Hines, C. A. Bower. Inorganic light-emitting diode displays using micro-transfer printing. *J. Soc. Inf. Disp.* **25**, 589-609 (2017).

[76] J. P. Lu, J. D. Thompson, G. L. Whiting, D. K. Biegelsen, S. Raychaudhuri, R. Lujan, J. Veres, L. L. Lavery, A. R. Völkel, E. M. Chow. Open and closed loop manipulation of charged microchiplets in an electric field. *Appl. Phys. Lett*. **105**, 054104 (2014).

[77] F. Caruso, M. Mosca, S. Rinella, R. Macaluso, C. Calì, F. Saiano, E. Feltin. Frequency-downconversion stability of PMMA coatings in hybrid white light-emitting diodes. *J. Electron. Mater.* **45**, 682-687 (2016).

[78] Y. –C. Lin, J. P. You, N. T. Tran, Y. He, F. G. Shi. Packaging of phosphor based

high power white LEDs: Effects of phosphor concentration and packaging configuration. *J. Electron. Packag*. **133**, 011009 (2011).

[79] H. –V. Han, H. –Y. Lin, C. –C. Lin, W. –C. Chong, J. –R. Li, K. –J. Chen, P. Yu, T. –M. Chen, H. –M. Chen, K. –M. Lau, H. –C. Kuo. Resonant-enhanced full-color emission of quantum-dot-based micro LED display technology. *Opt. Express* **23**, 32504-32515 (2015).

[80] R. Mupparapu, K. Vynck, T. Svensson, M. Burresi, D. S. Wiersma. Path length enhancement in disordered media for increased absorption. *Opt. Express* **23**, A1472-A1484 (2015).

[81] Z. Luo, H. Chen, Y. Liu, S. Xu, S. –T. Wu. Color-tunable light emitting diodes based on quantum dot suspension. *Appl. Opt*. **54**, 2845-2850 (2015).

[82] C.- H. Kim, J. –H. Bang, K. B. Hong, M. –H. Park. Fabrication of highly photoluminescent quantum dot-polymer composite micropatterned surface using thiol-ene chemistry. *RSC Adv*. **6**, 96700-96705 (2016).

[83] M. Duan, Z. Feng, Y. Wu, Y. Yin, Z. Hu, W. Peng, D. Li, S. –J. Chen, C. –Y. Lee, A. Lien. Inkjet-printed micrometer-thick patterned perovskite quantum dot films for efficient blue-to-green photoconversion. *Adv. Mater. Technol*. **4**, 1900779 (2019).

[84] M. J. Smith, C. H. Lin, S. Yu, V. V. Tsukruk. Composite structures with emissive quantum dots for light enhancement. *Adv. Opt. Mater.* **7**, 1801072 (2019).

[85] C. B. Murray, D. J. Norris, M. G. Bawendi. Synthesis and characterization of nearly monodisperse CdE (E = S, Se, Te) semiconductor nanocrystallites. *J. Am. Chem. Soc*. **115**, 8706-8715 (1993).

[86] E. Jang. Environmetally friendly quantum dots for display applications. in *IEEE International Electron Devices Meeting* (2018).

[87] D. Hahm, J. H. Chang, B. G. Jeong, P. Park, J. Kim, S. Lee, J. Choi, W. D. Kim, S. Rhee, J. Lim, D. C. Lee, C. Lee, K. Char, W. K. Bae. Design principle for bright, robust, and color-pure $InP/ZnSe_xS_{1-x}/ZnS$ heterostructures. *Chem. Mater.* **31**, 3476-3484 (2019).

[88] D. Hahm, J. Park, I. Jeong, S. Rhee, T. Lee, C. Lee, S. Chung, W. K. Bae, S. Lee. Surface engineered colloidal quantum dots for complete green process. *ACS Appl. Mater. Interfaces* **12**, 10563-10570 (2020).

[89] Y. –H. Won, O. Cho, T. Kim, D. –Y. Chung, T. Kim, H. Chung, H. Jang, J. Lee, D. Kim. E. Jang. Highly efficient and stable InP/ZnSe/ZnS quantum dot light-emitting diodes. *Nature* **575**, 634-638 (2019).

[90] V. Srivastava, V. Kamybayev, L. Hong, E. dunietz, R. F. Klie, D. V. Talapin. Colloidal chemistry in molten salts: Synthesis of luminescent $In_{1-x}Ga_xP$ and $In_{1-x}Ga_xAs$ quantum dots. *J. Am. Chem. Soc.* **140**, 12144-12151 (2018).

[91] H. Kang, S. Kim, J. H. Oh, H. C. Yoon, J. –H. Jo, H. Yang, Y. R. Do. Color-by-blue QD-emissive LCD enabled by replacing RGB color filters with narrow-band GR InP/ZnSeS/ZnS QD films. *Adv. Opt. Mater.* **6**, 1701239 (2018).

[92] H. M. haverinen, R. A. Myllylä, G. E. Jabbour. Inkjet printed RGB quantum dot-hybrid LED. *J. Disp. Technol.* **6**, 87-89 (2010).

[93] S. Lee, C. Lee. High-density quantum dots composites and its photolithographic patterning applications. *Polym. Adv. Technol.* **30**, 749-754 (2019).

[94] K. Fukada, T. Someya. Recent progress in the development of printed thin-film transistors and circuits with high-resolution printing technology. *Adv. Mater*. **29**, 1602736 (2017).

[95] K. Kim, G. Kim, B. R. Lee, S. Ji, S. –Y. Kim, B. W. An, M. H. Song, J. –U. Park. High-resolution electrohydrodynamic jet printing of small-molecule organic light-emitting diodes. *Nanoscale* **7**, 13410-13415 (2015).

[96] B. H. Kim, M. S. Onses, J. B. Lim, S. Nam, N. Oh, H. Kim, K. J. Yu, J. W. Lee, J. –H. Kim, S. –K. Kang, C. H. Lee, J. Lee, J. H. Shin, N. H. Kim, C. Leal, M. Shim, J. A. Rogers. High-resolution patterns of quantum dots formed by electrohydrodynamic jet printing of light-emitting diodes. *Nano Lett*. **15**, 969-973 (2015).

[97] V. Vespini, S. Coppola, M. Todino, M. Paturzo, V. Bianco, S. Grilli, P. Ferraro. Forward electrohydrodynamic inkjet printing of optical microlenses on microfluidic devices. *Lab. Chip* **16**, 326-333 (2016).

[98] X. Li, J. Shao, H. Tian, Y. Ding, X. Li. Fabrication of high-aspect-ratio microstructures using dielectrophoresis-electrocapillary force-driven UV-imprinting. *J. Micromech. Microeng*. **21**, 065010 (2011).

[99] A. Lee, H. Jin, H. –W. Dang, K. –H. Choi, K. H. Ahn. Optimization of experimental parameters to determine the jetting regimes in electrohydrodynamic printing. *Langmuir* **29**, 13630-13639 (2013).

[100] H. –K. Kim, B. Kim, J. –S. Kim, J. Park, Y. Lee, T. Jung, K. Lee, H. Jung, C. –R. Moon, J. Ahn, G. Hiroshige, C. –Y. Choi, D. Lee. Development of lensed color filter technology for higher SNR and lower crosstalk CMOS image sensor. in *IEEE Intl. Image Sensor Workshop* (2013).

[101] W. Li, R. A. Jones, S. C. Allen, J. C. Heikenfeld, A. J. Steckl. Maximizing Alq3 OLED internal and external efficiencies: Charge balanced device structure and color conversion outcoupling lenses. *J. Disp. Technol*. **2**, 143-152 (2006).

[102] T. –W. Koh, H. Cho, C. Yun, S. Yoo. ITO-free down-conversion white organic light-emitting diodes with structured color conversion layers for enhanced optical efficiency and color rendering. *Org. Electron*. **13**, 3145-3153 (2012).

[103] S. Mariani, V. Robbiano, R. Iglio, A. A. La Mattina, P. Nadimi, J. Wang, B. Kim, T. Kumeria, M. J. Sailor, G. Barillaro. Moldless printing of silicone lenses with embedded nanostructured optical filter. *Adv. Funct. Mater*. **30**, 1906836 (2020).

[104] C. Choi, A. R. Colón-Berríos, L. S. Hamachi, J. S. Owen, T. H. Schwartz, H. Ma, I. Kymissis. Localizing seizure activity in the brain using implantable micro-LEDs with quantum dot downconversion. *Adv. Mater. Technol*. **3**, 1700366 (2018).

[105] S. Lee, G. Kim, E. Oh, Y. Hong. Printed reflective sloped wall for enhancing luminance of color-conversion light source. *SID Symp. Dig. Tech. Papers* **50**, 1485-1487 (2019).

[106] S. -H. Eom, E. Wrzesniewski, J. Xue. Close-packed hemispherical microlens arrays for light extraction enhancement in organic light-emitting devices. *Org. Electron*. **12**, 472-476 (2011).

[107] B. Saha, W. Q. Toh, E. Liu, S. B. Tor, D. E. Hardt, J. Lee. A review on the importance of surface coating of micro/nano-mold in micro/nano-molding process. *J. Micromech. Microeng*. **26**, 013002 (2016).

[108] J. F. Oliver, C. Huh, S. G. Mason. Resistance to spreading of liquids by shape edges. *J. Colloid Interface Sci.* **59**, 568-581 (1977).

[109] S. Yasuda, K. Shimizu. Pinned square lens arrays and their application to integral photography. *Jpn. J. Appl. Phys*. **52**, 06GL03 (2013).

[110] J. Osinski. P. Palomaki. Quantum dot design criteria for color conversion in microLED displays. *SID Symp. Dig. Tech. Papers* **50**, 34-37 (2019).

[111] W. Tian, L. Dou, Z. Jin, J. Xiao, J. Li. Full-color micro-LED displays with cadmium-free quantum dots patterned by photolithography technology. *Appl. Opt*. **59**, 11112-11122 (2020).

[112] Q. Li, K. R. Westlake, M. H. Crawford, S. R. Lee, D. D. Koleske, J. J. Figiel, K. C. Cross, S. Fathololoumi, Z. Mi, G. T. Wang. Optical performance of top-down fabricated InGaN/GaN nanorod light emitting diode array. *Opt. Express* **19**, 25528-25534 (2011).

[113] K. –H. Jeong, J. Kim, L. P. Lee. Biologically inspired artificial compound eyes. *Science* **312**, 557-561 (2006).

[114] Y. M. Song, Y. Xie, V. Malyarchuk, J. Xiao, I. Jung, K. –J. Choi, Z. Liu, H. Park, C. Lu, R. –H. Kim, R. Li, K. B. Crozier, Y. Huang, J. A. Rogers. Digital cameras with designs inspired by the arthropod eye. *Nature* **497**, 95-99 (2013).

[115] G. J. Lee, C. Choi, D. –H. Kim, Y. M. Song. Bioinspired artificial eyes: Optic components, digital cameras, and visual prostheses. *Adv. Funct. Mater*. **28**, 1705202 (2018).

[116] Y. Wang, C. Shi, C. Liu, X. Yu, H. Xu, T. Wang, Y. Qiao, W. Yu. Fabrication and characterization of a polymeric curved compound eye. *J. Micromech. Microeng*. **29**, 055008 (2019).

[117] H. Liu, F. Chen, Q. Yang, P. Qu, S. He, X. Wang, J. Si, X. Hou. Fabrication of bioinspired omnidirectional and gapless microlens array for wide field-of-view detections. *Appl. Phys. Lett*. **100**, 133701 (2012).

[118] J. Li, W. Wang, X. Mei, A. Pan, X. Sun, B. Liu, J. Cui. Artificial compound eyes prepared by a combination of air-assisted deformation, modified laser swelling, and controlled crystal growth. *ACS Nano* **13**, 114-124 (2019).

[119] W. –K. Kuo, G. –F. Kuo, S. –Y. Lin, H. H. Yu. Fabrication and characterization of artificial miniaturized insect compound eyes for imaging. *Bioinspir. Biomim*. **10**, 056010 (2015).

[120] D. Shin, T. Huang, D. Neibloom, M. A. Bevan, J. Frechette. Multifunctional liquid marble compound lenses. *ACS Appl. Mater. Interfaces* **11**, 34478-34486 (2019).

[121] P. –S. Tsai, Y. –M. Yang, Y. –L. Lee. Hierarchically structured superhydrophobic coatings fabricated by successive Langmuir-Blodgett deposition of micro-/nano-sized particles and surface silanization. *Nanotechnology* **18**, 465604 (2007).

[122] N. N. Khanh, K. B. Yoon. Facile organization of colloidal particles into large, perfect one- and two-dimensional arrays by dry manual assembly on patterned substrates. *J. Am. Chem. Soc*. **131**, 14228-14230 (2009).

[123] C. Park, T. Lee, Y. Xia, T. J. Shin, J. Myoung, U. Jeong. Quick, large-area assembly of a single-crystal monolayer of spherical particles by unidirectional rubbing. *Adv. Mater*. **26**, 4633-4638 (2014).

[124] C. Park, K. Koh, U. Jeong. Structural color painting by rubbing particle powder. *Sci. Rep*. **5**, 8340 (2015).

[125] J. L. Wilbur, R. J. Jackman, G. M. Whitesides, E. L. Cheung, L. K. Lee, M. G. Prentiss. Elastomeric optics. *Chem. Mater.* **8**, 1380-1385 (1996).

[126] D. Chandra, S. Yang, P. –C. Lin. Strain responsive concave and convex microlens array. *Appl. Phys. Lett.* **91**, 251912 (2007).

[127] K. Wei, H. Zeng, Y. Zhao. Insect-human hybrid eye (IHHE): An adaptive optofluidic lens combining the structural characteristics of insect and human eyes. *Lab. Chip* **14**, 3594-3602 (2014).

[128] A. Shahini, H. Jin, Z. Zhou, Y. Zhao, P. –Y. Chen, J. Hua. M. M. –C. Cheng. Toward individually tunable compound eyes with transparent graphene electrode. *Bioinspir. Biomim.* **12**, 046002 (2017).

[129] D. Zhu, C. Li, X. Zeng, H. Jiang. Tunable-focus microlens arrays on curved surfaces. *Appl. Phys. Lett.* **96**, 081111 (2010).

[130] Z. –C. Ma, X. –Y. Hu, Y. –L. Zhang, X. –Q. Liu, Z. –S. Hou, L. –G. Niu, L. Zhu, B. Han, Q. –D. Chen, H. –B. Sun. Smart compound eyes enable tunable imaging. *Adv. Funct. Mater.* **29**, 1903340 (2019).

[131] S. Parsad, A. Kadambi, Y. Alwehaibi, C. M. Collier. Mechanically-tuned optofluidic lenses for in-plane focusing of light. *OSA Continuum* **2**, 2694-2703 (2019).

[132] J. Byun, B. Lee, E. Oh, H. Kim, S. Kim, S. Lee, Y. Hong. Fully printable, strain-engineered electronic wrap for customizable soft electronics. *Sci. Rep.* **7**, 45328 (2017).

[133] S. Damodara, D. George, A. K. Sen. Single step fabrication and characterization of PDMS micro lens and its use in optocapillary flow manipulation. *Sens. Actuator B* **227**, 383-392 (2016).

[134] P. I. Hsu, M. Huang, Z. Xi, S. Wagner, Z. Suo, J. C. Strum. Spherical deformation of compliant substrate with semiconductor device islands. *J. Appl. Phys.* **95**, 705-712 (2004).

[135] Z. Li, Y. Wang, J. Xiao. Mechanics of bioinspired imaging systems. *Theor. Appl. Mech. Lett*. **6**, 11-20 (2016).

[136] S. Lee, C. Jang, S. Moon, J. Cho. B. Lee. Additive light field displays: Realization of augmented reality with holographic optical element. *ACM Trans. Graph*. **35**, 60 (2016).

[137] G. Biwa, M. Doi, A. Yasuda, H. Kadota. Technologies for the crystal LED display system. *SID Symp. Dig. Tech. Papers* **50**, 121-124 (2019).

[138] S. Bäumer. *Handbook of Plastic Optics* (Wiley-VCH, 2010).

[139] S. Thiele, C. Pruss, A. M. herkommer, H. Giessen. 3D printed stacked diffractive microlenses. *Opt. Express* **27**, 35621-35630 (2019).

[140] G. Yoon, K. Kim, D. Huh, H. Lee, J. Rho. Single-step manufacturing of hierarchical dielectric metalens in the visible. *Nat. Commun.* **11**, 2268 (2020).

[141] K. Akşit, P. Chakravarthula, K. Rathinavel, Y. Jeong, R. Albert, H. Fuchs, D. Luebke. Manufacturing application-driven foveated near-eye displays. *IEEE Trans. Vis. Comput. Graph*. **25**, 1928-1939 (2019).

[142] S. –U. Kim, J. Kim, S. –D. Lee. Precise lens-on-lens architecture using selective wettability for image-depth representation. *Mol. Cryst. and Liq. Cryst*. **595**, 50-54 (2014).

[143] Y. Shen, Q. Zou, B. Wan, X. She, R. You, Y. Luo, C. Jin. High-contrast dynamic reflecting system based on pneumatic micro/nanoscale surface morphing. *ACS Appl. Mater. Interfaces* **13**, 1988-1999 (2021).

[144] S. Yu. Y. Tang. Z. Li, K. Chen. X. Ding. B. Yu. Enhanced optical and thermal performance of white light-emitting diodes with horizontally layered quantum dots phosphor nanocomposites. *Photon. Res*. **6**, 90-98 (2018).

[145] H. Menkara, R. A. Gilstrap, T. Morris, M. Minkara, B. K. Wagner, C. J. Summers. Development of nanophosphors for light emitting diodes. *Opt. Express* **19**, A972-A981 (2011).

[146] T. Maruyama, H. Hirata, T. furukawa, S. Maruo. Multi-material microstereolithography using a palette with multicolor photocurable resin. *Opt. Mater. Express* **10**, 2522-2532 (2020).

[147] J. Bae, S. Lee, J. Ahn, J. H. Kim, M. Wajahat, W. S. Chang, S. –Y. Yoon, J. T. Kim, S. K. Seol, J. Pyo. 3D-printed quantum dot nanopixels. *ACS Nano* **14**, 10993- 11001 (2020).

[148] S. Kang, S. –H. Lee, S. –D. Lee. Quantum dot patterns in moleculary ordered matrix for emissive displays with wide color gamut. *SID Symp. Dig. Tech. Papers* **51**, 1779-1782 (2020).

[149] A. Samusjew, M. Kartzer, A. Moser, C. Teichert, K. K. Krawczyk, T. Griesser. Inkjet printing of soft, stretchable optical waveguides through the photopolymerization of high-profile linear patterns. *ACS Appl. Mater. Interfaces* **9**, 4941-4947 (2017).

[150] A. C. Roy, A. Ghatak. Design of an adaptable optofluidic aspherical lens by using the elastocapillary effect. *Adv. Opt. Mater*. **2**, 874-878 (2014).

[151] S. –I. Bae, K. Kim, S. Yang, K. –W. Jang, K. –H. Jeong. Multifocal microlens arrays using multilayer photolithography. *Opt. Express* **28**, 9082-9088 (2020).

[152] W. –L. Liang, J. –G. Pan, G. –D. J. Su. One-lens camera using a biologically

based artificial compound eye with multiple focal lengths. *Optica* **6**, 326-334 (2019).

[153] D. Keum, K. –W. Jang, D. S. Jeon, C. S. H. Wang, E. K. Buschbeck, M. H. Kim, K. –H. Jeong. Xenos peckii vision inspires an ultrathin digital camera. *Light Sci. Appl*. **7**, 80 (2018).

[154] W. Wang, J. Li, R. Li, B. Li, X. Mei, X. Sun. Fabrication of hierarchical micro/nano compound eyes. *ACS Appl. Mater. Interfaces* **11**, 34507-34516 (2019).

[155] J. –J. Kim. Y. Lee, H. G. Kim, K. –J. Choi, H. –S. Kweon, S. Park, K. –H. Jeong. Biologically inspired LED lens from cuticular nanostructures of firefly lantern. *Proc. Natl. Acad. Sci. U.S.A*. **109**, 18674-18678 (2012).

[156] E. Finan, H. Mathis, K. Gagne, K. Purvin, M. Nofziger. Reaching audiences big and small: Holistic approach to optics outreach at the Wyant College of Optics Science. *Proc. SPIE* **11480**, 114800C (2020).

[157] E. N. Udofia, W. Zhou. 3D printed optics with a soft and stretchable optical material. *Addit. Manuf*. **31**, 100912 (2020).

[158] P. Milojkovic. M. P. Christensen. Review of multiscale optical design. *Appl. Opt*. **54**, 171-183 (2015).

Abstract in Korean (국문 초록)

일반적으로 제조 공정은 절삭 방식과 적층 방식으로 구분된다. 이 중에서 적층 방식 공정은 저비용 및 단시간으로 복잡한 형태의 구조를 만들 수 있어서 이에 대한 연구와 개발이 꾸준히 진행되어왔다. 특히 3D 프린팅은 적층 방식 공정 중에서 가장 대표적인 방법으로, 기계 부품 및 생체 기관 제조 등의 분야에서는 이미 상용화가 진행되고 있다. 하지만 전자 소자 및 광학 요소 분야에서의 3D 프린팅의 활용은 여전히 연구 개발 또는 시제품 제작 단계에 머무르고 있다. 특히 마이크로 렌즈, 컬러 필터 등이 3D 프린팅으로 응용할 수 있는 가장 가능성 있는 광학 요소로서 디스플레이 및 이미징 시스템에 널리 사용될 것으로 예상되지만 여전히 상용화를 위한 연구가 진행 중이다. 또한 3D 프린팅을 이용한 광학 요소의 제작은 소재, 길이 스케일, 형상 및 응용 방안 등에서도 제한이 많은 상황이다. 따라서 이러한 문제를 극복하기 위해서는 디스플레이 및 이미징 시스템에서의 3D 프린팅 된 광학 요소의 유용성을 확장해야 하며, 다음과 같이 세 가지 측면에서 향상된 성능을 달성해야 한다. 첫째, 다양한 방식의 3D 프린팅 방법을 통해 마이크로미터에서 센티미터까지 광범위의 길이 스케일을 가지는 구조물의 제작이 가능해야 한다. 둘째, 임의의 곡면, 계층적 구조 등 복잡한 형상의 구조물을 쉽게 제작할 수 있어야 한다. 셋째, 단단한 소재 대신 탄성체와 같은 소프트 소재를 이용하여 광학적인 기능을 용이하게 조절할 수 있어야 한다.

이와 같은 동기를 바탕으로 본 학위 논문에서는 디스플레이 및 이미징 시스템으로의 응용을 위한 3D 프린팅 기반 맞춤형 광학 요소의 개발에 대한 내용을 보고한다. 3D 프린팅 기반 광학 요소를 매크로 스케일, 마이크로 스케일 그리고 매크로 및 마이크로 스케일이 혼합된 계층적 구조 등 세 가지 유형으로 분류하고 각각에 대한 응용 분야를 제시한다. 매크로 스케일의 광학 요소로는 가장 기본적인 요소인 렌즈와 거울을 선택한다. 렌즈는 공압식 디스펜싱 방법을 이용하여 실린드리컬 쌍 형태로 제작되었으며, 심리스 모듈러 평판식 디스플레이의 구현을 위해 적용된다. 또한 용융 적층 방식의 3D 프린팅으로 만들어진 몰드를 이용하여 거울을 제작하고, 이를 이용하여 심리스 모듈러 커브드 엣지 디스플레이를 구현한다. 이와 같이 모듈러 디스플레이의 이음새 부분에 3D 프린팅으로 제작된 렌즈 또는 거울을 부착하는 방식으로 화면을 심리스로 확장하는 기술을 제시하고, 다양한 형태의 디스플레이에 적용할 수 있는 가능성을 보여준다. 마이크로 스케일의 광학 요소로는 발광 다이오드에서 색 변환과 광 추출 기능을 동시에 나타내는 색 변환 마이크로 렌즈를 선택한다. 양자 점/광 경화성 고분자 복합체의 전기수력학적 프린팅을 통해 양자 점이 내장된 다양한 형태의 색 변환 마이크로 렌즈를 제작하며, 이를 청색 마이크로 발광 다이오드 어레이의 발광부 상에 적용하여 풀 컬러 마이크로 발광 다이오드 디스플레이로의 응용 가능성을 제시한다. 마지막으로 매크로 및 마이크로 스케일이 혼합된 계층적 구조의 광학 요소로서 디스펜싱 및 건식 러빙 과정의 조합으로 제작된 겹눈 형태를 모

사한 렌즈 구조를 제시한다. 반구 형태의 매크로 렌즈를 디스펜싱으로 형성하고, 매크로 렌즈의 곡면 상에 단층의 마이크로 입자의 배열을 얻기 위해 건식 러빙 공정을 진행한다. 이러한 방식으로 형성된 계층적 구조가 소프트한 소재로 복제되어서 신축성을 가지는 겹눈 형태 모사 구조가 완성된다. 마이크로 렌즈 어레이는 매크로 렌즈의 표면을 따라 형성되고 리지드 아일랜드로 역할을 하여, 전체 계층적 구조에 기계적 변형이 가해져 매크로 렌즈의 모양이 변형되어도 마이크로 렌즈는 형상과 해상도, 초점 거리 등의 광학적 특성을 유지할 수 있다.

본 학위 논문은 3D 프린팅을 이용하여 다양한 형태와 스케일의 광학 요소를 제작하고 디스플레이 및 이미징 시스템으로의 여러 응용을 보여줌으로서 앞으로의 새로운 연구 및 개발 방향성을 제시하는 것을 주요 목적으로 한다. 3D 프린팅 설비의 단가가 낮아지고 정밀도 및 해상도가 높아지는 추세에 따라, 광학 요소를 쉽게 만들고 응용할 수 있는 '맞춤형 광학' 또는 '스스로 구현하는 광학' 분야가 변형 가능하고 멀티 스케일의 광학계로 점차 확대될 것으로 예상된다. 궁극적으로는 차세대 디스플레이 및 이미징 시스템에 필요한 광학 요소를 위한 기술의 저변을 넓히고, 이를 산업 전반에 응용할 수 있는 기반을 마련하고자 한다.

주요어: 3D 프린팅, 광학 요소, 디스플레이 및 이미징 시스템, 렌즈, 거울, 컬러 필터, 겹눈 모사 구조

학번: 2014−21610